



# Optimization of the hot working parameters of a nickel-based superalloy using a constitutive-dynamic recrystallization model and three-dimensional processing map

Xiaoyun Feng<sup>1,2</sup>, Lianxi Hu<sup>1,2,\*</sup> , and Yu Sun<sup>1,2,\*</sup>

<sup>1</sup> National Key Laboratory for Precision Hot Processing of Metals, Harbin Institute of Technology, Harbin 150001, People's Republic of China

<sup>2</sup> School of Materials Science and Engineering, Harbin Institute of Technology, Harbin 150001, People's Republic of China

Received: 28 March 2021

Accepted: 15 June 2021

Published online:

1 July 2021

© The Author(s), under exclusive licence to Springer Science+Business Media, LLC, part of Springer Nature 2021

## ABSTRACT

The hot deformation characteristics of hot-pressed nickel-based superalloy were investigated by employing hot compression experiments over the temperatures range of 1050–1200 °C and the strain rates range of 0.001–10 s<sup>-1</sup> under true strain of 0.7. The constitutive relationship was established considering Zener–Hollomon parameter, dynamic recrystallization (DRX) critical model and kinetic model based on the flow stress data corrected by friction and adiabatic heating. The hot deformation activation energy was calculated to be 577.45 kJ/mol, the results show that the flow stress predicted by the constitutive equation is in good agreement with the experimental data, and the DRX kinetic model matched well with the microstructure analyzed by electron backscatter diffraction technique. The three-dimensional distribution of power dissipation efficiency taking the influence of strain into account and processing maps were constructed to further delineate the intrinsic workability of alloy. Combined with microstructure observation, it is recommended that the optimum hot working windows were identified in the samples deformed within 1160–1190 °C / 0.05–0.819 s<sup>-1</sup>, 1130–1165 °C / 0.0025–0.05 s<sup>-1</sup> and 1055–1085 °C / 0.011–0.135 s<sup>-1</sup>; homogeneous and fine equiaxed microstructures can be found in this domain mainly due to the appearance of DRX.

Handling Editor: P. Nash.

Address correspondence to E-mail: hulx@hit.edu.cn; yusun@hit.edu.cn

<https://doi.org/10.1007/s10853-021-06276-4>

## Introduction

Nickel-based superalloy EP741NP precipitation strengthened by  $\gamma'$  ( $\text{Ni}_3(\text{Al,Ti})$ ) phase with ordered  $\text{L1}_2$  structure in disordered face-centered-cubic (FCC)  $\gamma$  matrix is broadly used to prepare high-performance rotating components of advanced aero-engine due to excellent creep performance and superior mechanical properties at elevated temperature [1]. In spite of the advantages mentioned above, the application of EP741NP superalloy in aviation industry is still restricted due to the presence of a large number of alloying elements such as W, Mo, Co, Cr in this alloy. It inevitably increases the difficulty of hot deformation and narrow the hot processing window to a certain extent. It is generally accepted that flow behavior of materials during hot working is highly affected by microstructures which in turn depend on the processing parameters like temperature, strain rate and strain. In addition, the hot working of the alloy with low stacking fault energy is associated with work hardening (WH), dynamic recovery (DRV) and dynamic recrystallization (DRX) and other metallurgical mechanisms, which also has an important effect on the microstructure of deformed samples [2, 3]. Hence, in order to optimize the processing parameters and conduct the hot processing at suitable deformation conditions, it is imperative to investigate the influence of deformation parameters on hot deformation behavior by establishing appropriate constitutive relationship and processing map. The flow behavior of metallic materials during hot deformation process usually reflects the evolution of the internal microstructure of the alloy. The rheological behavior of the alloy is related to the hot deformation process parameters such as temperature, strain rate and strain. In order to quantitatively describe the relationship between flow stress and thermal deformation parameters, the researchers proposed the flow stress constitutive model theory. In recent years, in view of different materials and different rheological characteristics, most researchers have adopted the phenomenological models (Arrhenius model and Johnson–Cook model) to establish the constitutive relationship during the hot deformation [4, 5]. In addition, Arrhenius model contains a number of model parameters with physical meaning, which can better express the relationship between flow stress and deformation parameter, and is more

widely used. Recently, considerable researches for nickel-based superalloy have been carried out on constitutive equation based on Arrhenius hyperbolic-sine model. Lin et al. [6] predicted the hot deformation behavior of a nickel-based superalloy based on microstructural evolution and constitutive models. Pu et al. [7] investigated the deformation characteristics of UNS10276 superalloy at temperatures of 950–1250 °C and strain rates between 0.01–10  $\text{s}^{-1}$ . Wu et al. [8] conducted flow behavior of FGH96 superalloy under the conditions of temperatures range of 1020–1110 °C and strain rates range of 0.001–1  $\text{s}^{-1}$ , combined with finite element simulation to analyze the microstructure and deformation distribution in the compression samples. Wang et al. [9] established the activation energy map of Inconel 740 superalloy based on Arrhenius equations to characterize the hot workability. It is well known that hot deformation is a process of competition between work hardening and flow softening. However, it should be noted that the flow softening mechanism in the previously established constitutive relationship of nickel-based superalloys has not been fully considered. Besides, the use of inappropriate process parameters in hot working process of alloys can lead to macroscopic or microscopic structure defects, thereby reducing the utilization of materials. For the determination of the optimal hot processing window for the material, the processing map is regarded as an effective and practical technique. The dynamic material model has become the most widely used model for the determination of the flow instability zone in plastic forming process and the optimization of the hot deformation parameters. The processing map is obtained by superimposing the instability map and the power dissipation map. In the power dissipation diagram, the thermal processing area of the alloy is optimized by introducing power dissipation efficiency. The value of power dissipation efficiency is related to the proportion of energy converted into heat during the thermal processing. The larger the value, the more energy is used for the transformation of the alloy shape and microstructure during the hot deformation, which means the higher the thermal processing efficiency under this process parameter. The hot deformation process of the alloy not only depends on the energy utilization efficiency, but also is related to the rheological instability behavior. In recent years, many scholars have used the dynamic material model to establish the processing map of the

nickel-based superalloy during hot deformation. D. Wen et al. [10] developed the processing map of the aged nickel-based superalloy, and correlated with the deformed microstructures. O. Lypchanskyi et al. [11] investigated the evaluation of hot workability of nickel-based superalloy using processing maps. So far, compared with the traditional two-dimensional (2D) processing map, the three-dimensional (3D) processing map has been adopted by most scholars because it can more intuitively reveal the influence of strain [12–16].

In present work, a constitutive model is established by comprehensively considering the work hardening and flow softening behaviors in hot deformation of EP741NP superalloy over wide ranges of deformation temperature and strain rate. The 3D power dissipation efficiency and processing maps are studied, and the relationship between the microstructure and processing map is illustrated.

## Experimental procedures and materials

The nickel-based superalloy EP741NP with chemical composition of Co 14.55, Cr 8.36, W 5.68, Mo 4.25, Al 2.92, Nb 2.82, Ti 1.60, Si 0.81, F 0.68, Cl 0.36, Hf 0.27 and Fe 0.25, rest Ni (wt%) was studied in this research. This studied alloy was manufactured by powder metallurgy processes, including plasma rotating electrode process (PREP) and vacuum hot pressing (HP). The powders with diameter in the range of 45–106  $\mu\text{m}$  were hot-pressed at 1205  $^{\circ}\text{C}$  and the pressure of 50 MPa for 1 h. The microstructure of the original material from experimentally as-HPed superalloy is shown in Fig. 1. It can be seen that the microstructure of as-HPed samples consists of equiaxed grains with large size together with fine grains dispersed along the grain boundaries or prior powder particles, and the average grain size is approximately 83.30  $\mu\text{m}$ . Generally, based on misorientation angle ( $\theta$ ) between adjacent grains, the high-angle grain boundaries (HAGBs) and low-angle grain boundaries (LAGBs) are considered to be  $\theta \geq 15^{\circ}$  and  $2^{\circ} \leq \theta \leq 15^{\circ}$ , respectively. It can be seen from Fig. 1 that the fraction of HAGBs with the misorientation angle greater than  $15^{\circ}$  is high, and only a small amount of LAGBs can be observed. Besides, it can be seen from Fig. 1e that the  $\gamma'$  phase with a size range from 1 to 10  $\mu\text{m}$ , which are usually

exhibited either in a block morphology or an elongated morphology.

The cylindrical samples with 12 mm in height and 8 mm in diameter were electrical discharge machined from as-HPed compacts. Isothermal hot compression tests were conducted on Gleeble 3800 thermo-mechanical simulator at the strain rate range of 0.001–10  $\text{s}^{-1}$  with an interval of one order of magnitude, the temperature range of 1050–1200  $^{\circ}\text{C}$  with an interval of 30  $^{\circ}\text{C}$  and the samples are subjected to 50% reduction in height accounting to true strain of 0.7. The graphite sheets with a thickness of 0.05 mm were placed between the sample and anvil to minimize the friction effect and ensure the uniform of compression. As shown in Fig. 2, all samples were heated to the designated deformation temperature at a rate of 10  $^{\circ}\text{C}/\text{s}$  and held for 5 min to reduce the thermal gradient before deformation. The samples were immediately quenched in water so as to maintain the hot deformation microstructure at the end of deformation.

The deformed samples were cut parallel to the compression axis, followed by mechanical polished and chemically etched in Kalling's reagent (5gCuCl<sub>2</sub>, 100 ml hydrochloric acid, 100 ml ethanol) for optical metallographic observation. The samples for electron backscatter diffraction (EBSD) examination were electrolytically etched with a solution of 20 ml H<sub>2</sub>SO<sub>4</sub> and 80 ml CH<sub>3</sub>OH at a voltage of 20 V for 30 s. The samples for transmission electron microscopy microscope (TEM) analysis were firstly ground to foils with a thickness less than 50  $\mu\text{m}$  and then thinned by a twin-jet electro-polished (10 pct perchloric acid and 90 pct ethanol) at -20  $^{\circ}\text{C}$  under 50–75 V.

## Results and discussion

### Correction of friction and adiabatic heating effect on flow stress curves

#### Correction of friction

The friction between specimen and compression dies is inevitable during the thermal simulation compression experiment. The graphite lubricant was utilized to reduce the friction in hot deformation experiment; however, it still cannot completely eliminate the friction effect. The existence of friction significantly increase the flow stress of the material,

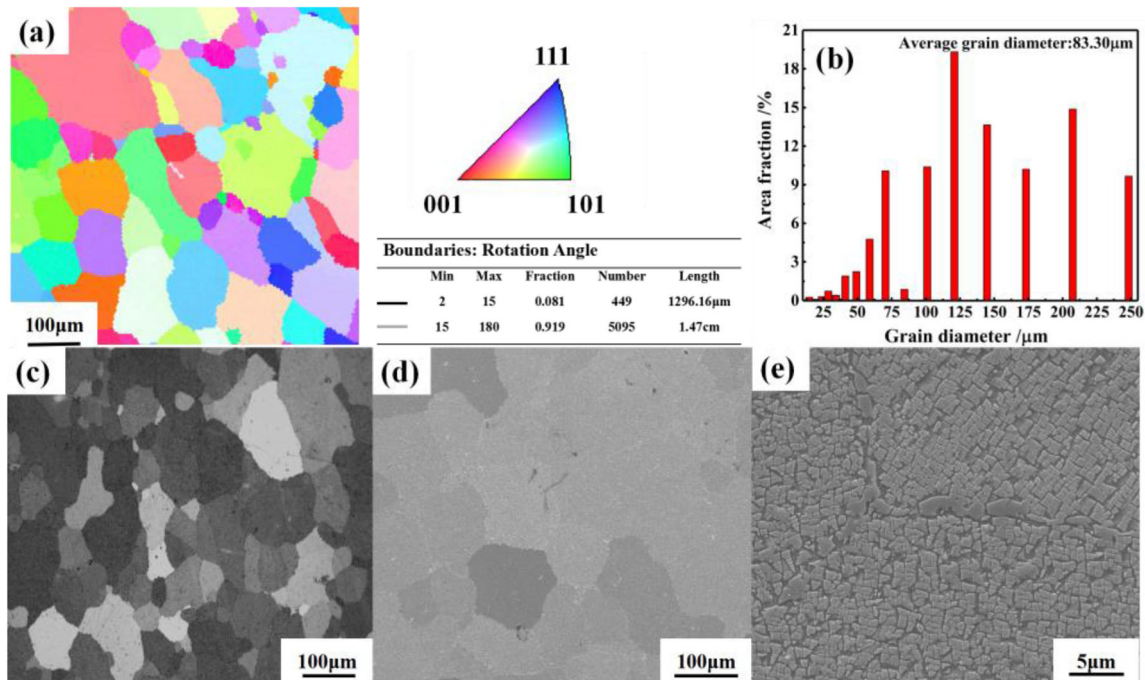


**Figure 1** Microstructure, grain size distribution and  $\gamma'$  phase of as-HPed EP741NP superalloy.

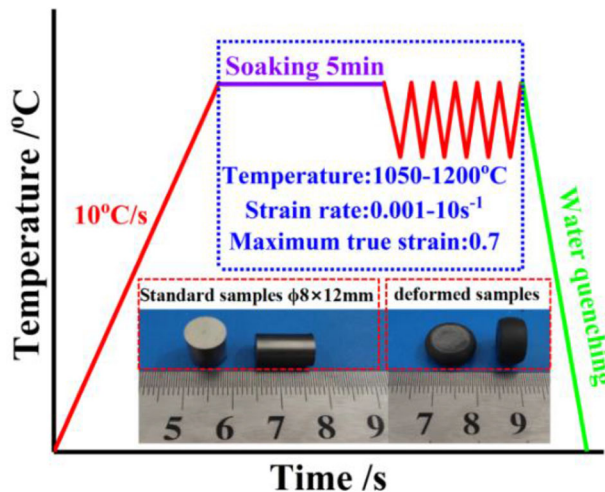


**Figure 2** The schematic depiction of hot compression experiments.

so that the material inhomogeneous deformation occurs in the hot deformation, resulting in an obvious deviation between the flow stress experimentally obtained and the true stress of material. Therefore, the friction correction model proposed by Ebrahimi et al. [17] was adopted to calibrate the flow stress experimentally obtained under different hot deformation conditions. The relationship between the

corrected flow stress ( $\sigma_c$ ) and experimentally obtained flow stress ( $\sigma_e$ ) can be depicted as follows:

$$\frac{\sigma}{\sigma_f} = \frac{8br}{h} \left\{ \left[ \frac{1}{12} + \left( \frac{h}{rb} \right)^2 \right]^{3/2} - \left( \frac{h}{rb} \right)^3 - \frac{f \exp(-b/2)}{24\sqrt{3}(\exp(-b/2) - 1)} \right\} \quad (1)$$

where  $\sigma$  is the experimentally measured flow stress,  $\sigma_f$  is the flow stress corrected by friction,  $f$  is the constant friction factor,  $b$  is barrel parameter, and  $r$  and  $h$  are average radius and height of samples after hot compression, respectively. Based on Eq. (1), it can be found that  $f$  and  $b$  play a key role in the correction of flow stress, which can be described as follows:

$$f = 3\sqrt{3}rb/[h(12 - 2b)] \quad (2)$$

$$b = (4h/r)[(r_m - r_t)/(h - h_0)] \quad (3)$$

where  $r = r_0(h_0/h)^{1/2}$ ,  $r_0$  and  $h_0$  are initial radius and height of samples before hot compression,  $r_m$  and  $r_t$  ( $r_t = [3h_0r_0^2/h - 2r_m^2]^{1/2}$ ) are the maximum and top radius of deformed samples.

#### Correction of adiabatic heating effect

The phenomenon that flow stress curves showing a downward trend after the stress peak due to dynamic softening may be attributed to the deformation heat and microstructure changes. The hot deformation of the alloy at a low strain rate is considered to be an



isothermal condition, while a high strain rate is regarded as an adiabatic condition because the specimen does not have sufficient time for heat exchange. Consequently, it is necessary to remove the adiabatic heating effect in flow stress curves at high strain rate. An analytical model suggested by Gotez et al. [18] that establishes the relationship between temperature rise and flow stress was used to correct flow curves. Corrected flow stress  $\sigma_c$  can be expressed as follows:

$$\sigma_c = \sigma_f + \Delta T \left( \frac{d\sigma_f}{dT} \right) \Big|_{\epsilon, \dot{\epsilon}} \quad (4)$$

$$\Delta T = \frac{0.95\eta \int_0^\epsilon \sigma_f d\epsilon}{\rho C_p} \quad (5)$$

$$\eta = \left\{ 1 + \frac{\epsilon}{[(x_w/K_w) + (1/HTC) + (x_D/K_D)]x_w\rho C_p \dot{\epsilon}} \right\} \quad (6)$$

where  $\eta$  is adiabatic correction factor,  $\rho$  is the density of EP741NP superalloy (8.35 g/cm<sup>3</sup>), and  $C_p$  is the specific heat (5.9 × 10<sup>2</sup> J·kg<sup>-1</sup>·K<sup>-1</sup>),  $x_w$  is half of the deformed samples height,  $x_D$  is the distance from the die surface to the die interior where temperature is constant (0.015 m),  $K_w$  is thermal conductivity of deformed samples (23.0 W·mK<sup>-1</sup>),  $K_D$  is thermal conductivity of the die (21.0 W·mK<sup>-1</sup>),  $HTC$  is the interface heat-transfer coefficient (3 × 10<sup>4</sup> W·m<sup>-2</sup>·K<sup>-1</sup>), and  $\epsilon$  is experimentally measured strain [19, 20]. The corrected flow stress curves due to friction and adiabatic heating effects at the strain rate of 10 s<sup>-1</sup> are shown in Fig. 3. It can be seen from Fig. 3a that the flow stress corrected by friction effect is

lower than the value measured in the hot deformation experiment on account of the increase of deformation resistance. In addition, as the strain increases, the contact area between the deformed samples and the die increases, so that the difference in flow stress before and after friction correction increases, which is consistent with the result obtained by Wan et al. [21]. As seen from Fig. 3b, the flow stress curves displays a similar tendency, i.e., as the temperature rises and the strain rate decreases, the flow stress of deformed samples gradually decreases. the comparison of the curves after friction corrected and the curves after friction and adiabatic heating corrected. It should be noted that as the hot deformation temperature rises, the adiabatic heating effect of EP741NP superalloy weakened. Besides, it can be seen that the true stress–strain curves obtained in this experiment are relatively smooth, and there is no obvious serrated fluctuation, but the phenomenon of serrated flow (Portevin–Le Chatelier effect) in the flow stress curves obtained from experiment has also been reported [22, 23].

The flow stress curves of EP741NP superalloy before and after friction and temperature correction at different temperatures and strain rates are shown in Fig. 4. It is widely accepted that the flow stress of most alloys decreases as the deformation temperature increases and the strain rate decreases. The alloy has larger atomic kinetic energy at a higher temperature, and a lower strain rate ensures sufficient time for the completion of dynamic recrystallization. The flow stress curves shown in Fig. 4 is basically consistent with the above law. During the hot deformation of materials, there are mainly two mechanisms of work

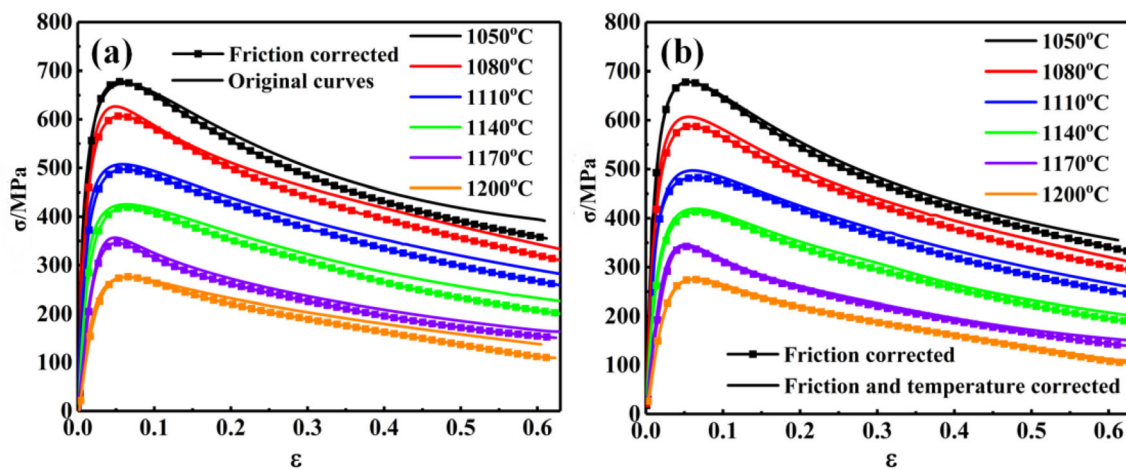
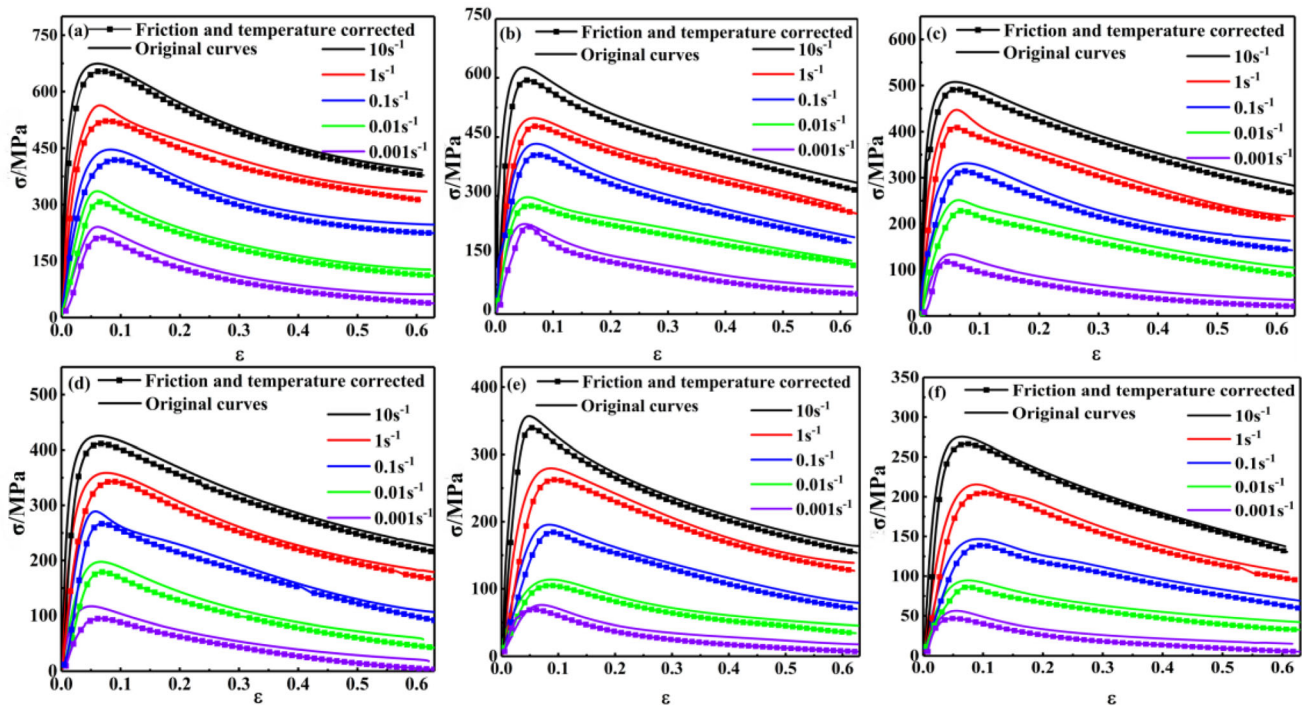


Figure 3 Corrected flow stress curves by friction and adiabatic heating effects at the strain rate of 10 s<sup>-1</sup>.



**Figure 4** Comparisons between the friction and temperature corrected and original flow stress curves at different conditions: **a** 1050 °C, **b** 1080 °C, **c** 1110 °C, **d** 1140 °C, **e** 1170 °C, **f** 1200 °C.

hardening and dynamic softening. The dynamic softening mechanism consists of dynamic recovery and dynamic recrystallization. The hot deformation behavior of materials can be regarded as a process in which the two mechanisms of work hardening and dynamic softening compete with each other. When the strain is small, the flow stress increases rapidly with the increase of the strain, which is due to the work hardening effect caused by the accumulation of dislocations at this stage. As the strain continues to increase, some dislocations annihilate to form a substructures, triggering a dynamic recovery effect. At this time, the work hardening effect of alloy still occupies the dominant position. The flow stress increases with the increases of the strain, but the rate of increase decreases. Then dynamic recrystallization occurs, the influence of dynamic softening gradually increases, the flow stress reaches a peak, and dynamic softening becomes the dominant mechanism during hot deformation. Therefore, the flow stress curves show a trend that flow stress decreases as the strain increases. In the end, the two mechanisms reach a dynamic equilibrium, and the flow stress remains unchanged as the strain increases.

## Constitutive modeling

### Zener–Holloman parameter

It is well known that the establishment of constitutive model is of great significance to the hot processing of alloys. The flow stress is greatly affected by temperature and strain rate, and peak stress can be selected as representative stress for calculation. Considering the comprehensive effects of temperature and strain rate in hot deformation, the Zener–Hollomon parameter ( $Z$ ) also known as the temperature compensated strain rate factor can be utilized to explain the hot deformation behavior of EP741NP superalloy, as expressed by following equations:

$$Z = \dot{\varepsilon} \exp\left(\frac{Q}{RT}\right) = f(\sigma_p) = \begin{cases} A_1 \sigma_p^{n_1} & \text{for } \alpha \sigma_p < 0.8 \\ A_2 \exp(\beta \sigma_p) & \text{for } \alpha \sigma_p > 1.2 \\ A [\sinh(\alpha \sigma_p)]^n & \text{for all } \sigma_p \end{cases} \quad (7)$$

where  $Q$  is the apparent activation energy ( $\text{J}\cdot\text{mol}^{-1}$ ),  $R$  is the universal gas constant ( $8.314 \text{ J}\cdot\text{mol}^{-1}\cdot\text{K}^{-1}$ ),  $\dot{\varepsilon}$  is strain rate ( $\text{s}^{-1}$ ),  $T$  is the absolute deformation temperature ( $\text{K}$ ),  $\sigma_p$  is the peak stress,  $A$ ,  $A_1$ ,  $A_2$ ,  $n_1$ ,  $\alpha$  and  $\beta$  are material constant, and  $n$  is stress exponent. As shown in Eq. (7), the relationship between  $Z$

parameter and peak stress can be depicted by power, exponential and hyperbolic sine equations. Among them, the power law applies to lower stress levels, while the exponential type is suitable for relatively high stress levels. In comparison, the hyperbolic sine equation can well characterize the relationship between hot deformation parameters and flow stress at any stress level due to the parameter  $\alpha$  has been optimized by the least squares method, which can be given as  $\alpha = \beta/n_1$ . Taking the natural logarithm of Eq. (7):

$$\text{Ln}Z = \begin{cases} \text{Ln}\dot{\epsilon} + \frac{Q}{RT} = \text{Ln}A_1 + n_1 \text{Ln}\sigma_p \\ \text{Ln}\dot{\epsilon} + \frac{Q}{RT} = \text{Ln}A_2 + \beta\sigma_p \\ \text{Ln}\dot{\epsilon} + \frac{Q}{RT} = \text{Ln}A + n \text{Ln}[\sinh(\alpha\sigma_p)] \end{cases} \quad (8)$$

Material constants  $n_1$ ,  $\beta$  and  $n$  can be calculated by taking partial differential on both sides of Eq. (8) at a given deformation temperature, as shown in the following equations:

$$n_1 = \left[ \frac{\partial \text{Ln}\dot{\epsilon}}{\partial \text{Ln}\sigma_p} \right]_T, \beta = \left[ \frac{\partial \text{Ln}\dot{\epsilon}}{\partial \sigma_p} \right]_T, n = \left[ \frac{\partial \text{Ln}\dot{\epsilon}}{\partial \text{Ln}[\sinh(\alpha\sigma_p)]} \right]_T \quad (9)$$

The parameters of  $n_1$  and  $\beta$  can be obtained by fitting the corrected flow stress data, as shown in Fig. 5a and b, with the mean values of  $n_1 = 7.034$  and  $\beta = 0.0281$ , respectively. Thus, the material constant  $\alpha = \beta/n_1 = 0.003995 \text{ MPa}^{-1}$  and the stress exponent  $n$  can be acquired by linear regression from Fig. 5c. For a given strain rate, taking partial differential of Eq. (8) and combining Eq. (9), the activation energy can be expressed as follows:

$$Q = Rn \left[ \frac{\partial \text{Ln}[\sinh(\alpha\sigma_p)]}{\partial (1/T)} \right]_{\dot{\epsilon}} = R \left[ \frac{\partial \text{Ln}\dot{\epsilon}}{\partial \text{Ln}[\sinh(\alpha\sigma_p)]} \right]_T \left[ \frac{\partial \text{Ln}[\sinh(\alpha\sigma_p)]}{\partial (1/T)} \right]_{\dot{\epsilon}}$$

It can be seen from Fig. 5c that the value of stress exponent is 3.851, which is similar to other nickel-based superalloys [24, 25]. The activation energy  $Q$  is available as  $577.45 \text{ kJ}\cdot\text{mol}^{-1}$ , which can be determined by the slope of  $\text{Ln}[\sinh(\alpha\sigma_p)]$  vs.  $1/T$ . The value of  $Q$  in this work is greater than the deformation activation energy of  $448.05 \text{ kJ/mol}$  in FGH96 superalloy by Wu et al. [8], of  $406.5 \text{ kJ/mol}$  in Inconel 718 superalloy by Tan et al. [26], and of  $373.86 \text{ kJ/mol}$  in Inconel 740 superalloy by Wang et al. [9]. It may be

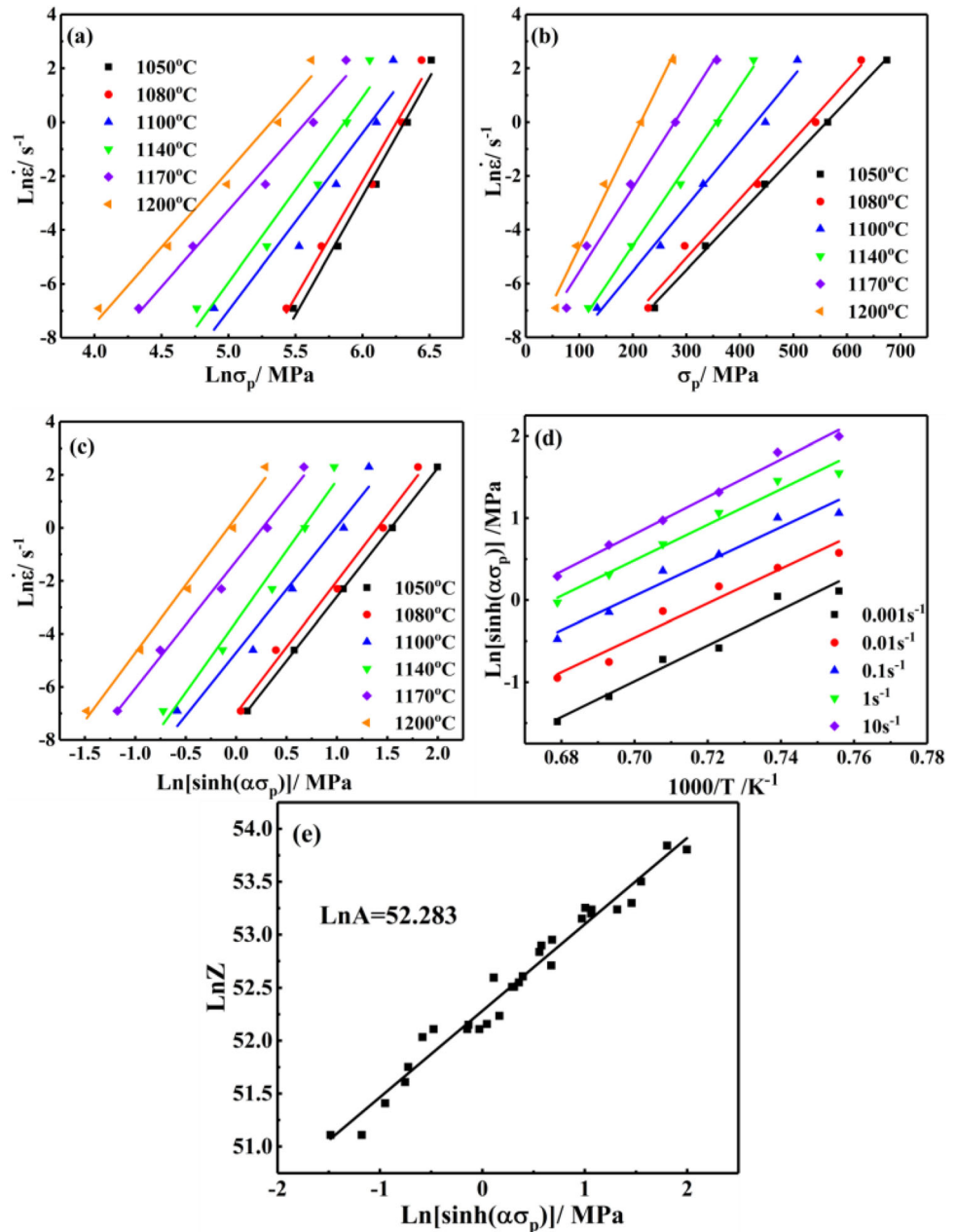
mainly related to the Hf, Mo, W solution strengthening elements with high melting point and large atomic radius in the alloy, which is not conducive to lattice diffusion [27]. Moreover, the  $\gamma'$  phase also plays a pivotal role in delaying or hindering the rearrangement of dislocations during dynamic recrystallization [25]. Compared with the above-mentioned superalloys, the content of  $\gamma'$  phase in EP741NP superalloy is higher, which can reach more than 60% due to the alloy contains high Ti, Al and other  $\gamma'$  phase forming elements. Therefore, substituting the acquired value of parameters  $A$ ,  $\alpha$ ,  $n$  and  $Q$ , the temperature compensated strain rate factor can be expressed as follows:

$$Z = \dot{\epsilon} \exp(577450/RT) = 5.081 \times 10^{22} [\sinh(0.003995\sigma_p)]^{3.581} \quad (11)$$

### Dynamic recrystallization critical model

It is widely accepted that the response of alloy to applied pressure during hot compression is the product of competition between work hardening and dynamic softening (dynamic recovery and dynamic recrystallization) of deformed specimens. Generally, both of two kinds of primary mechanism are influenced by temperature and strain rate; the flow stress increases with increasing strain rate and decreasing temperature. In the present work, the flow stress curves are considered to be the net results of the simultaneous action of dynamic recovery (DRV) and dynamic recrystallization (DRX). During hot deformation, DRX occurs when the dislocation density inside the material reaches a certain critical value [28]. The effect of DRX on grains refinement and improvement of material properties is not negligible. It is essential to determine the critical occurrence model of DRX, since the evolution of the microstructure can be predicted and simulated [15]. The critical condition of DRX can be determined by observing the microstructure using metallographic method or analyzing the flow stress curves. Compared with the metallographic method, which requires observation of a large number of samples and with which it is difficult to accurately estimate the critical conditions for the formation of new grains, simple and fast analysis of the flow stress curve is obviously more suitable. In order to determine the critical conditions for DRX in flow stress curves, the work hardening rate ( $\theta = d\sigma/d\epsilon$ ) proposed by

**Figure 5** Plots of  $\sigma_p, T$  and  $\dot{\epsilon}$ : **a**  $\text{Ln}\dot{\epsilon} - \text{Ln}\sigma_p$ , **b**  $\text{Ln}\dot{\epsilon} - \sigma_p$ , **c**  $\text{Ln}\dot{\epsilon} - \text{Ln}[\sinh(\alpha\sigma_p)]$ , **d**  $\text{Ln}[\sinh(\alpha\sigma_p)] - 1000/T$  and **e**  $\text{Ln}Z - \text{Ln}[\sinh(\alpha\sigma_p)]$ .



McQueen and Ryan [29] was applied to the present work, describing the relationship between the rate of flow stress and strain. The curves between work hardening rate ( $\theta$ ) and flow stress ( $\sigma$ ) are drawn by using the corrected flow stress data, which can further understand the work hardening behavior of the alloy. Poliak and Jonas [30, 31] point out that due to the occurrence of DRX, the inflection point that appears on the work hardening curve is the critical point of DXR, as expressed in following equation.

$$\frac{\partial}{\partial \sigma} \left( \frac{\partial \theta}{\partial \sigma} \right) = 0 \tag{12}$$

At this time, the deformation storage energy caused by dislocation multiplication, plugging and entanglement reaches the maximum and the rate of energy consumption is the smallest [32]. Figure 6 displays the curves ( $\theta - \sigma$ ) and ( $\sigma - \epsilon - \theta$ ) at the temperature of 1110 °C and the strain rate of 0.01 s<sup>-1</sup> for EP741NP superalloy.

The strain at the beginning of DRX in Fig. 6 is the critical strain ( $\epsilon_c$ ) and the corresponding stress is the



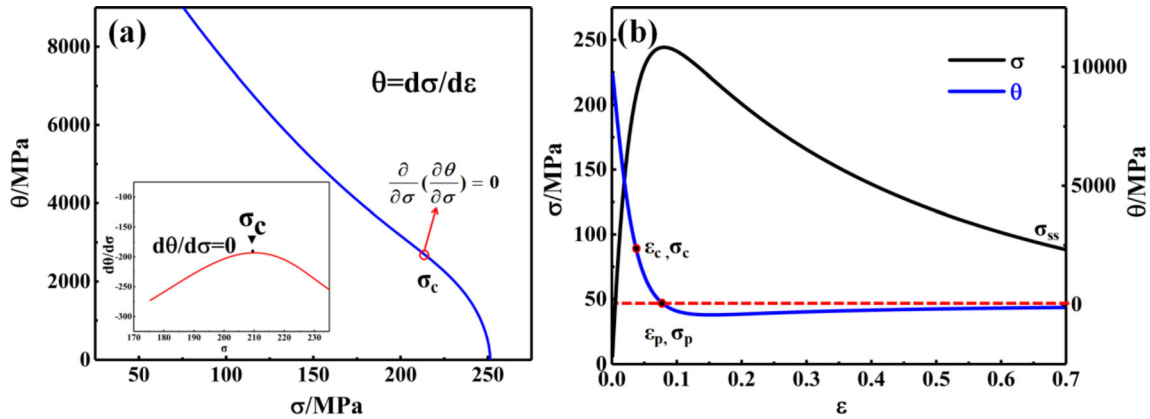


**Figure 6** The work hardening curves of EP741NP superalloy at 1110 °C/0.01 s<sup>-1</sup> **a**  $\theta - \sigma$  and **b**  $\sigma - \varepsilon - \theta$ .

critical stress ( $\sigma_c$ ), which can be determined by the second derivative of  $\theta$  relative to  $\sigma$  is zero (i.e.,  $\partial^2\theta / \partial\sigma^2 = 0$ ). The peak stress ( $\sigma_p$ ) and the peak strain ( $\varepsilon_p$ ) are calculated with the point at which the work hardening rate  $\theta$  falls to zero, where  $\sigma_{ss}$  is stress when the dynamic recrystallization flow stress curves reach the steady state. According to the same method as above, the work hardening curves of EP741NP superalloy under different deformation conditions can be obtained, as shown in Fig. 7.

By repeating the above method, the characteristic parameter ( $\sigma_c, \varepsilon_c, \sigma_p, \varepsilon_p, \sigma_{ss}$ ) values under each hot deformation condition can be obtained. The relationship between the natural logarithm of stress ( $\sigma$ ), strain ( $\varepsilon$ ) and the hot deformation parameter ( $Z$ ) is shown in Fig. 8.

Consequently, the DRX critical model of EP741NP superalloy is described in the following equations.

$$\begin{cases} \sigma_p = 2.339\sigma_c^{0.87} \\ \sigma_p = 0.00003Z^{0.32} \end{cases} \quad (13)$$

$$\begin{cases} \varepsilon_p = 1.44\varepsilon_c^{0.99} \\ \varepsilon_p = 0.0034Z^{0.06} \end{cases} \quad (14)$$

*Dynamic recrystallization kinetic model*

There are two typical flow stress curves of DRV and DRX during hot deformation, and the initial stages of the two curves are coincident. Before the critical point of DRX, the DRV constitutive equation can be used to describe the stress–strain relationship. After the critical point, the DRX curves drop significantly. The flow stress difference between the two curves is defined as  $\Delta\sigma$  here, which mainly depends on the volume fraction of DRX ( $X_{DRX} = \Delta\sigma / (\sigma_{sat} - \sigma_{ss})$ ). The constitutive model proposed by J. Jonas et al. [33] in

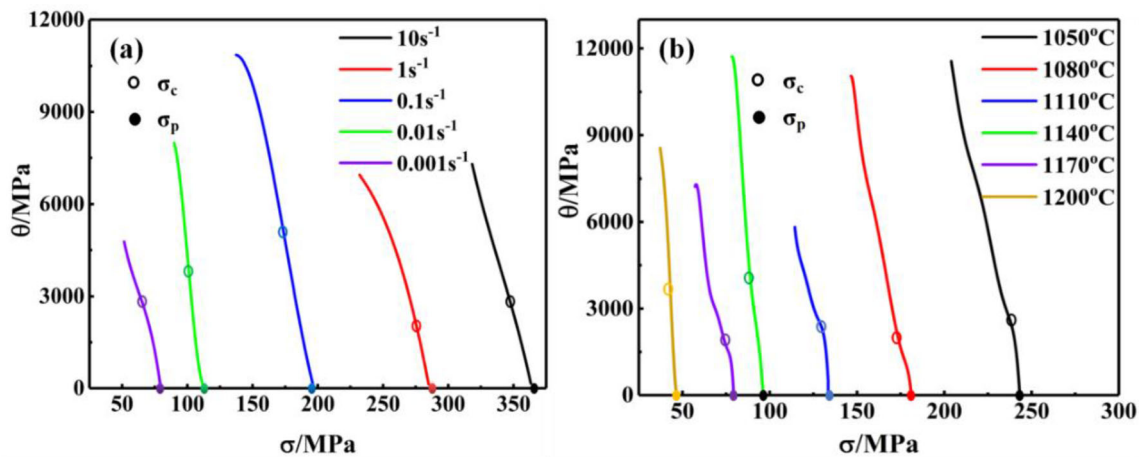


**Figure 7** The work hardening curves at different conditions: **a** 1170 °C and **b** 0.001 s<sup>-1</sup>.

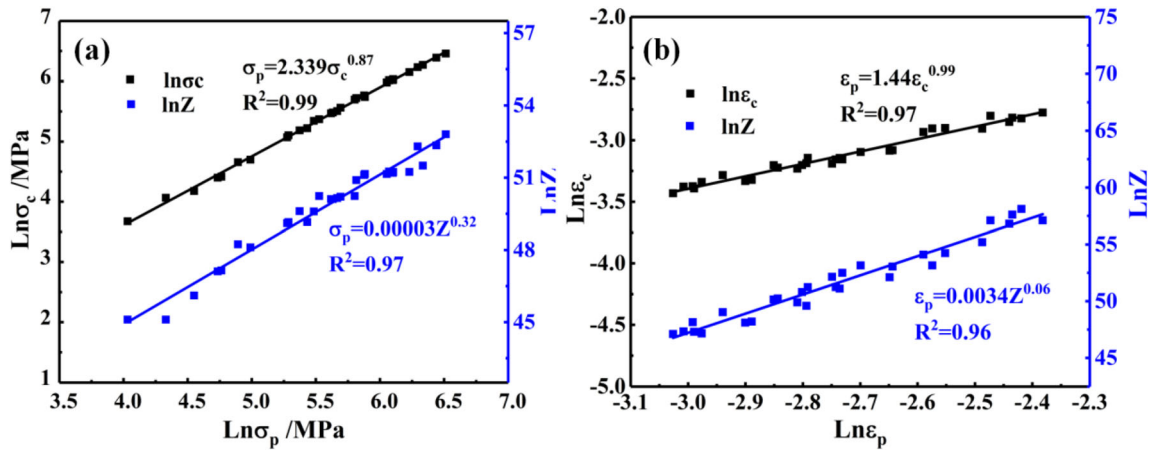


**Figure 8** The relationship among critical parameter, peak parameter and Z parameter: **a** Ln  $\sigma_c$  – Ln Z and **b** Ln  $\epsilon_c$  – Ln Z.

hot deformation is used in the present work, which can be described as follows:

$$\begin{cases} \sigma = [\sigma_{sat}^2 + (\sigma_{0.2}^2 - \sigma_{sat}^2) \exp(-r(\epsilon - \epsilon_{0.2}))]^{1/2}, \epsilon < \epsilon_c \\ \sigma = [\sigma_{sat}^2 + (\sigma_{0.2}^2 - \sigma_{sat}^2) \exp(-r(\epsilon - \epsilon_{0.2}))]^{1/2} - X_{DRX}(\sigma_{sat} - \sigma_{ss}), \epsilon \geq \epsilon_c \end{cases} \quad (15)$$

$$\sigma\theta = 0.5r\sigma_{sat}^2 - 0.5r\sigma^2 \quad (16)$$

where  $\sigma_{0.2}$  is the yield strength corresponding to a total strain offset about 0.2%,  $\epsilon_{0.2}$  is corresponding strain,  $\sigma_{sat}$  represents the asymptotic stress value corresponding to the saturation of the flow stress curve, when there is only DRV softening during hot deformation.  $r$  is the coefficient of dynamic recovery at a constant temperature and strain rate. Based on Eq. 16, the values of  $\sigma_{sat}$  and  $r$  can be determined by plotting the curve of  $\theta\sigma - \sigma^2$ , as exhibited in Fig. 9. The

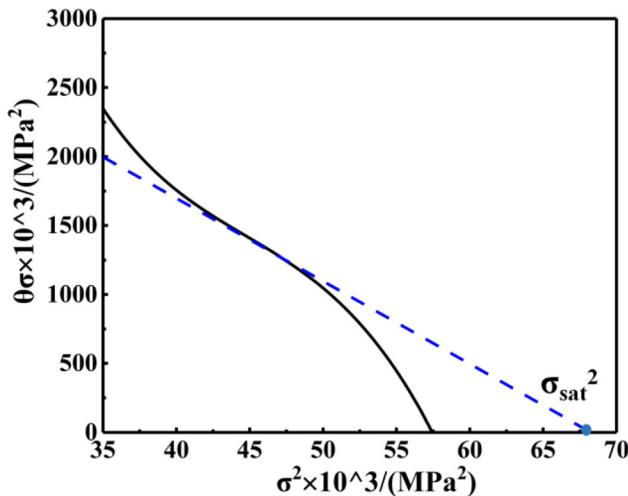


**Figure 9** The curve of  $\theta\sigma - \sigma^2$  of EP741NP superalloy at 1110 °C/0.01 s<sup>-1</sup>.

value of  $r$  can be calculated from the slope of the tangent at the curve inflection point ( $d(\theta\sigma)/d(\sigma^2)$ ), and  $\sigma_{sat}$  is defined using the extrapolation of the  $\theta\sigma - \sigma^2$  curves to  $\theta\sigma = 0$ .

The DRX kinetic model of EP741NP superalloy can be established by using the modified Avrami equation proposed by Laasraoui and Serajzadeh [34, 35] as expressed in Eq. 17, which can predict the DRX behavior under different hot working parameters.

$$X_{DRX} = 1 - \exp\{-k[(\epsilon - \epsilon_c)/\epsilon_p]^n\} \quad (17)$$

Taking the natural logarithm of Eq. 16:

$$\ln[-\ln(1 - X_{DRX})] = \ln k + n \ln[(\epsilon - \epsilon_c)/\epsilon_p] \quad (18)$$

The values of  $n$  and  $k$  can be obtained by the relationship between  $\ln[-\ln(1 - X_{DRX})]$  and  $\ln[(\epsilon - \epsilon_c)/\epsilon_p]$  at given temperature and strain rate, where  $n$  and  $\ln k$  represent the slope and the intercept, respectively. Therefore, the DRX kinetics model can be determined by taking the average value of  $n$  and  $k$  calculated under all deformation parameter in the present work, which can be expressed as follows:

$$\begin{cases} X_{DRX} = 0, \epsilon < \epsilon_c \\ X_{DRX} = 1 - \exp\{-0.2344[(\epsilon - \epsilon_c)/\epsilon_p]^{1.2566}\}, \epsilon \geq \epsilon_c \end{cases} \quad (19)$$

In order to express the characteristic parameters obtained above more conveniently, a mathematical expression relationship is established between characteristic parameters and the peak stress that can be accurately measured, as shown in Fig. 10. It can be seen that the matching results that is more

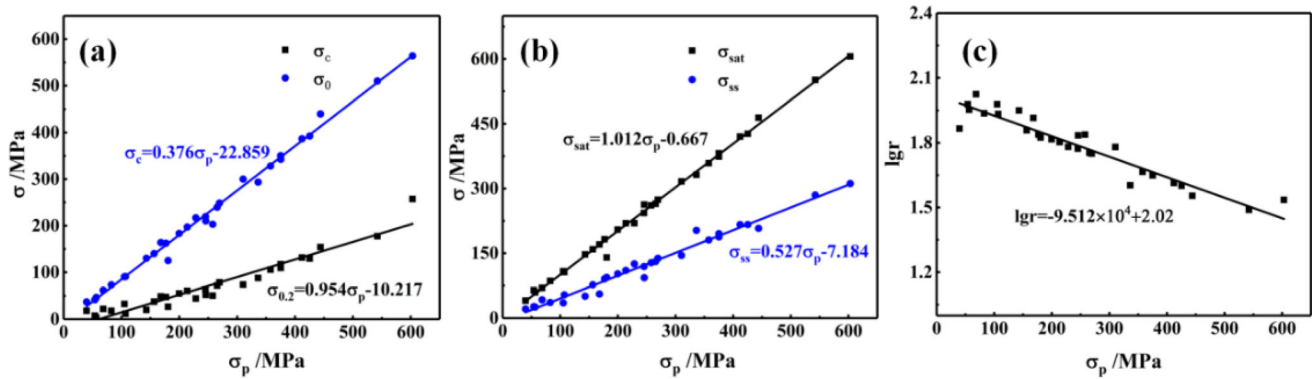


Figure 10 The relationship between characteristic parameters and the peak stress: a  $\sigma_c$ ,  $\sigma_{0.2}$ , b  $\sigma_{sat}$ ,  $\sigma_{ss}$ , c r.

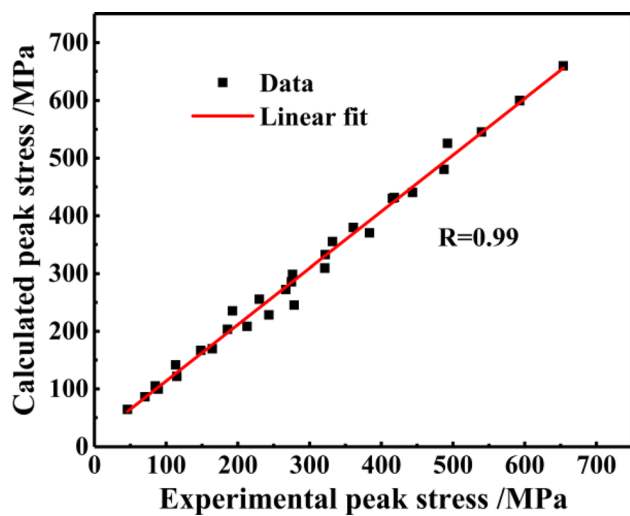


Figure 11 Comparison between experimental and calculated peak stress of EP741NP superalloy.

suitable with the data are described in the following equations:

$$\begin{cases} \sigma_c = 0.376\sigma_p - 22.859 \\ \sigma_{0.2} = 0.954\sigma_p - 10.217 \\ \sigma_{sat} = 1.012\sigma_p - 0.667 \\ \sigma_{ss} = 0.527\sigma_p - 7.184 \\ \lg r = -9.512 \times 10^{-4}\sigma_p + 2.02 \end{cases}$$

In summary, a constitutive equation that can completely characterize the flow behavior of EP741NP superalloy composed of the expression of the temperature compensated strain rate factor, the DRX critical occurrence model and kinetic model is constructed, which can be described as follows:

$$\begin{cases} \sigma = [\sigma_{sat}^2 + (\sigma_{0.2}^2 - \sigma_{sat}^2)\exp(-r(\epsilon - \epsilon_{0.2}))]^{1/2}, \epsilon < \epsilon_c \\ \sigma = [\sigma_{sat}^2 + (\sigma_{0.2}^2 - \sigma_{sat}^2)\exp(-r(\epsilon - \epsilon_{0.2}))]^{1/2} - X_{DRX}(\sigma_{sat} - \sigma_{ss}), \epsilon \geq \epsilon_c \end{cases}$$

$$\begin{cases} X_{DRX} = 0, \epsilon < \epsilon_c \\ X_{DRX} = 1 - \exp\{-0.2344[(\epsilon - \epsilon_c)/\epsilon_p]^{1.2566}\}, \epsilon \geq \epsilon_c \\ \begin{cases} \sigma_p = 2.339\sigma_c^{0.87} \\ \sigma_p = 0.00003Z^{0.32} \end{cases} \begin{cases} \epsilon_p = 1.44\epsilon_c^{0.99} \\ \epsilon_p = 0.0034Z^{0.06} \end{cases} \\ \begin{cases} \sigma_c = 0.376\sigma_p - 22.859 \\ \sigma_{0.2} = 0.954\sigma_p - 10.217 \\ \sigma_{sat} = 1.012\sigma_p - 0.667 \\ \sigma_{ss} = 0.527\sigma_p - 7.184 \\ \lg r = -9.512 \times 10^{-4}\sigma_p + 2.02 \end{cases} \end{cases} \quad (21)$$

$$\begin{aligned} Z &= \dot{\epsilon} \exp(577450/RT) \\ &= 5.081 \times 10^{22} [\sinh(0.003995\sigma_p)]^{3.581} \end{aligned}$$

In order to evaluate the constitutive equation established in present work, the correlation coefficient (R) and the average absolute relatively error (AARE) are employed, as described in Eq. 22 [36]. The comparison results of peak stresses between experimental values and calculated values are exhibited in Fig. 11.

$$\begin{aligned} R &= \frac{\sum_{n=1}^{i-1} (\sigma_{exp}^i - \bar{\sigma}_{exp})(\sigma_p^i - \bar{\sigma}_p)}{\sqrt{\sum_{n=1}^{i-1} (\sigma_{exp}^i - \bar{\sigma}_{exp})^2 \sum_{n=1}^{i-1} (\sigma_p^i - \bar{\sigma}_p)^2}} \\ AARE &= \frac{1}{n} \sum_{i=1}^n \left| \frac{\sigma_{exp}^i - \sigma_p^i}{\sigma_{exp}^i} \right| \end{aligned} \quad (22)$$

where  $\sigma_{exp}^i$  and  $\sigma_p^i$  are the experimental and calculated stress,  $\bar{\sigma}_{exp}^i$  and  $\bar{\sigma}_p^i$  are the average vales, respectively, and n is the number of data. The values of R and AARE are 99% and 8.73%, separately. The high value of R and low value of AARE indicate the established constitutive model can well characterize the flow behavior of EP741NP superalloy in the deformation temperature range of 1050–1200 °C and strain rate of 0.001–10 s<sup>-1</sup>.

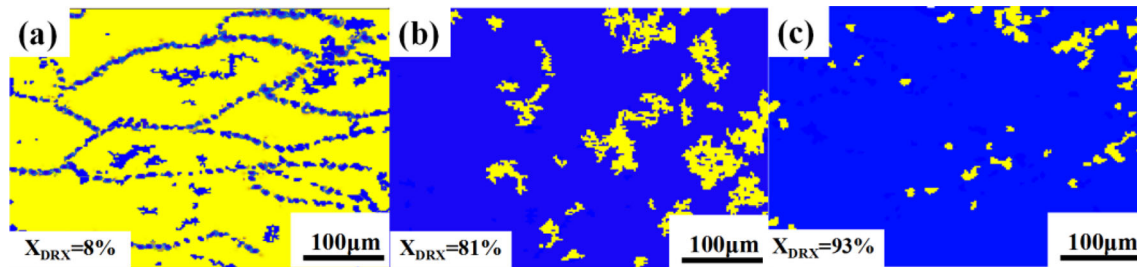


**Figure 12** The microstructure of specimens deformed at 1080 °C/0.001 s<sup>-1</sup> under different strain: **a**  $\varepsilon = 0.1$ , **b**  $\varepsilon = 0.5$ , and **c**  $\varepsilon = 0.7$ .

Based on the theory of metal dislocations, dislocations are packed and entangled when metal is deformed, resulting in a larger number of sub-grain boundaries, while the dynamic recrystallized grain has a smaller deformation and fewer internal sub-grain boundaries. Therefore, it can be concluded that the volume fraction of deformed grains decreases as the deformation increases, and the volume fraction of dynamic recrystallized grains increases. Counting the number of sub-grain boundaries inside the samples through OIM software can intuitively describe the change of the parameter dynamic recrystallization volume fraction ( $X_{DRX}$ ). The DRX kinetics model included in constitutive equation is verified by EBSD analysis results at different hot deformation parameters, as shown in Figs. 13 and 14. Dynamic recrystallized grains and deformed grains are represented by different colors. In Figs. 13 and 14, blue represents dynamic recrystallized grains and yellow represents deformed grains. Figure 13 shows the microstructure of specimens deformed at 1080 °C/0.001 s<sup>-1</sup> under different strain. It is explicitly from Fig. 12 that the volume fraction of DRX increases with increasing strain. The evolution of DRX volume fraction at different temperatures and strain rates with the strain of 0.3 is presented in Fig. 13. It can be seen that the volume fraction of DRX increases with decreasing of strain rate at a fixed strain. Comparing the above DRX volume fraction calculated by OIM software with established DRX kinetic model (Fig. 14), it is found that the two are in good agreement.

### Establishment of 3D processing maps

To evaluate the hot workability at different deformation conditions and predict the optimum processing parameters of EP741NP superalloy during hot deformation, the processing maps are investigated in this work. Processing maps are established

by superimposing the instability map on the power dissipation map, based on the dynamic materials model (DMM) proposed by Prasad et al. [37–40], which present the effect of deformation temperature and strain rate on the microstructure at a given strain. According to the irreversible thermodynamics principle, the workpiece is considered as a power dissipation system, where the total input power  $P$  consists of the power dissipation arising from plastic deformation (represented by content  $G$ ) and metallurgical processes (represented by co-content  $J$ ) related to the energy concerning the microstructure evolution. Thus, the relationship among  $P$ ,  $G$  and  $J$  can be expressed as follows:

$$P = \sigma \dot{\varepsilon} = G + J = \int_0^{\dot{\varepsilon}} \sigma d\dot{\varepsilon} + \int_0^{\sigma} \dot{\varepsilon} d\sigma \quad (23)$$

The partition of powder  $G$  and  $J$  depends on the strain rate sensitivity ( $m$ ), which is given as:

$$m = \frac{dJ}{dG} = \frac{\dot{\varepsilon} d\sigma}{\sigma d\dot{\varepsilon}} = \left[ \frac{\partial(Ln\sigma)}{\partial(Ln\dot{\varepsilon})} \right]_{\varepsilon, T} \quad (24)$$

For a given deformation temperature and strain,  $J$  co-content can be simplified to:

$$J = \int_0^{\sigma} \dot{\varepsilon} d\sigma = \frac{\sigma \dot{\varepsilon} m}{m + 1} \quad (25)$$

when  $m = 1$ , the workpiece is considered as an ideal linear dissipator, and the energy  $J$  reaches the maximum to be  $J_{max} = P/2$ . However, for a nonlinear dissipative process, a dimensionless parameter called the power dissipation efficiency  $\eta$  is introduced to evaluate the power dissipation capacity of the alloy, represented as:



**Figure 13** The evolution of  $X_{DRX}$  at different temperatures and strain rates with the strain of 0.3: **a** 1140 °C/10 s<sup>-1</sup>, **b** 1140 °C/1 s<sup>-1</sup>, **c** 1140 °C/0.1 s<sup>-1</sup> and **d** 1140 °C/0.01 s<sup>-1</sup>.

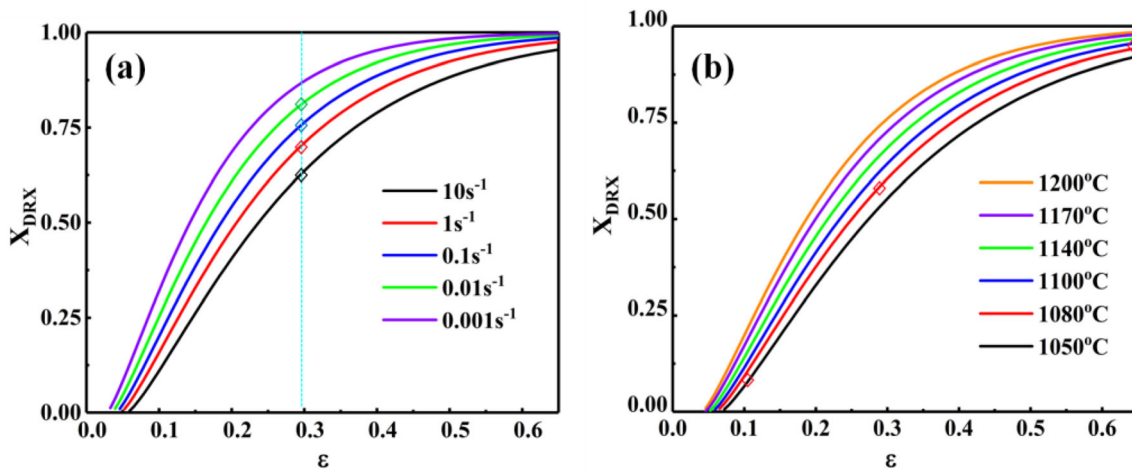
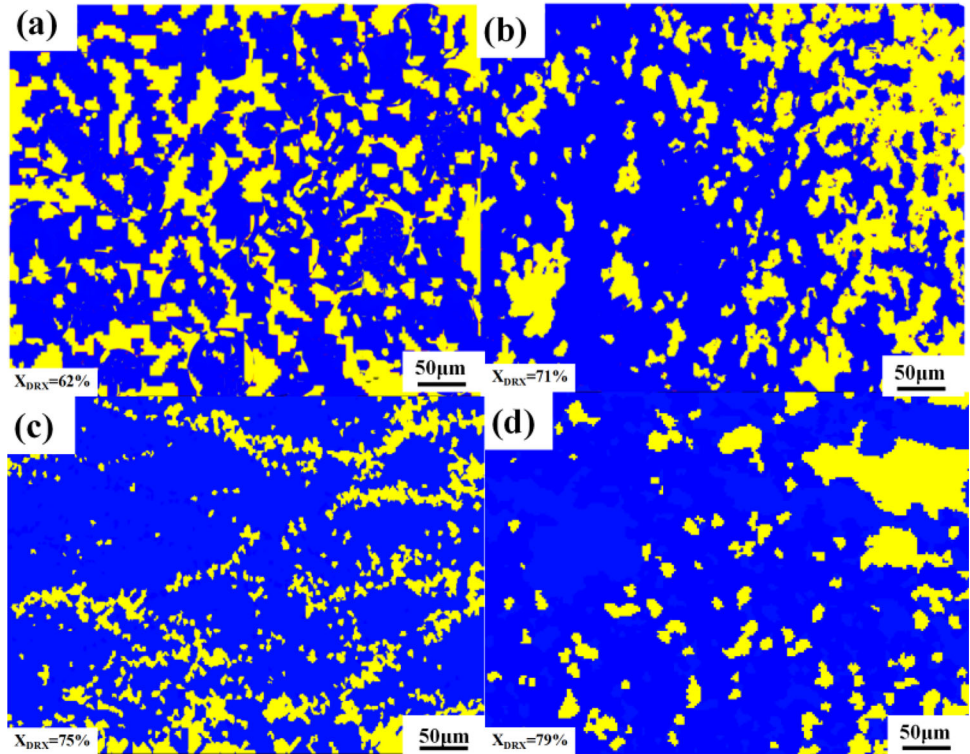


**Figure 14** The relationship between  $X_{DRX}$  and  $\epsilon$  at different conditions: **a** 1140 °C **b** 0.001 s<sup>-1</sup>.

$$\eta = \frac{J}{J_{max}} = \frac{2m}{m + 1} \tag{26}$$

The power dissipation maps are constituted by the variation of the power dissipation efficiency ( $\eta$ ) with deformation temperature and strain rate, which directly demonstrate the corresponding microstructure mechanism to a certain extent. It is acknowledged that domains with higher  $\eta$  in power dissipation map are supposed to be the optimum

processing conditions associated with DRX, DRV and superplasticity. Besides, the flow instability caused by damage mechanisms, including adiabatic shear bands, crack formation, deformation twinning and dynamic strain aging, etc., should be considered [41]. To distinguish the flow instability domains of alloy, the instability criterion proposed by Prasad et al. [42] based on the extremum principle of irreversible thermodynamics applied to large plastic deformation. The flow instability criteria  $\zeta$  is expressed as:

$$\xi(\dot{\epsilon}) = \frac{\partial \ln[m/(m+1)]}{\partial \ln \dot{\epsilon}} + m \leq 0 \quad (27)$$

The variation of  $\xi$  with deformation temperature and strain rate is used to develop the instability maps. It can be inferred from Eq. 27 that the instability domains are depicted by the negative value of  $\xi$ .

### Evolution of 3D power dissipation efficiency with strain

The response of power dissipation efficiency ( $\eta$ ) to different processing parameters including deformation temperature, strain rate and strain is shown in Figs. 15 and 16. Thereinto, Fig. 15 displays two-dimensional (2D) contour maps of power dissipation efficiency at different temperature and strain rate arranged along the rising strain axis to form three-dimensional (3D) slice diagrams. In order to further explore the influence of deformation parameters on power dissipation efficiency, the evolution of 3D distribution of  $\eta$  combined with the 2D planar skeleton map is shown in Fig. 16. As expected, strain has a significant effect on the power dissipation efficiency map. This is mainly due to the fact that the energy stored inside the sample may accumulate with the increase of dislocations, but it may be consumed by the annihilation of dislocations and microstructure variations [14]. Considering Figs. 15 and 16, it is clearly seen from these images that the lower power dissipation efficiency value being less than 20% mainly distributed in four deformation regions. The first one is primarily occurred in the range of 1090–1140 °C and 0.1–1 s<sup>-1</sup> when the initial

strain is 0.1 and this region disappear with an increase in strain up to 0.6. The second region is located in higher deformation temperatures and higher strain rates (1160–1200 °C, 2.718–10 s<sup>-1</sup>) at the strain of 0.2. The lower  $\eta$  value is also found in higher deformation temperatures and lower strain rates (1065–1110 °C, 0.001–0.0067 s<sup>-1</sup>) identified as third deformation region, and this region gradually expands with the increase of strain. The smallest  $\eta$  value in this region is concentrated in the temperature range of 1070–1090 °C and the strain rate of 0.001 s<sup>-1</sup>. The fourth region is distributed in the range of 1170–1200 °C and 0.001–0.0067 s<sup>-1</sup> when the true strain reaches 0.7. Besides, the higher power dissipation efficiency value is mainly focused on the higher temperatures (1150–1170 °C) and lower strain rates (0.001–0.1 s<sup>-1</sup>), and the maximum  $\eta$  value in this region moves toward the lowest strain rate (0.001 s<sup>-1</sup>) with the proceeding of strain. When the strain is greater than 0.4, the higher  $\eta$  value varying in the range of 33%–52% appears in the strain rate range of 0.001–0.0067 s<sup>-1</sup> at a lower temperature of 1050 °C.

The 3D power dissipation efficiency map constituted by 2D contours in the different coordinates (strain rate–temperature, strain rate–strain and strain–temperature) is presented in Fig. 17. At a given strain rate of 0.001 s<sup>-1</sup>, the higher  $\eta$  value occurs in the temperature range of 1140–1170 °C and strain range of 0.5–0.7. In addition, for strain ranging from 0.3–0.7, the higher  $\eta$  value is also found at temperature of 1050 °C. The lower  $\eta$  value is concentrated in medium temperature range of 1080–1100 °C and higher temperature range of 1170–1200 °C. The  $\eta$  values have obvious fluctuations

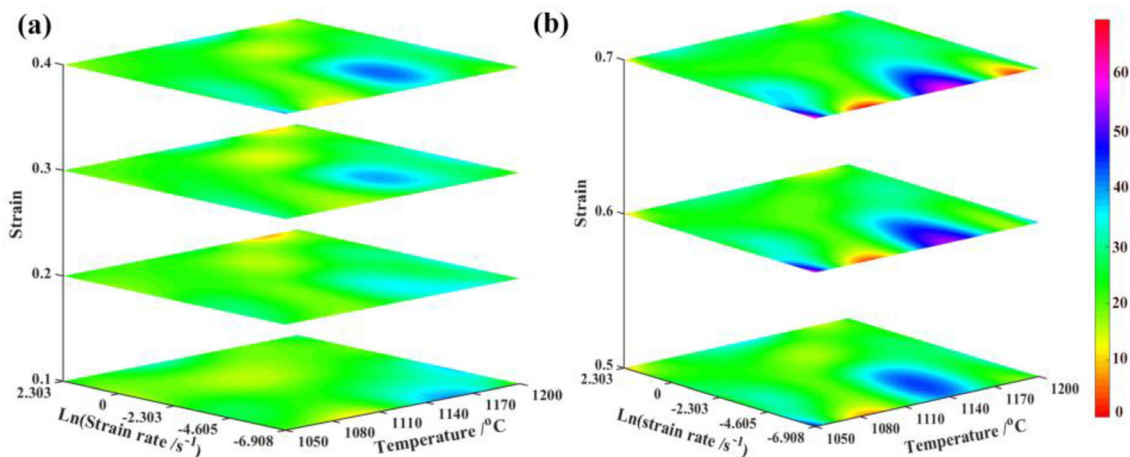
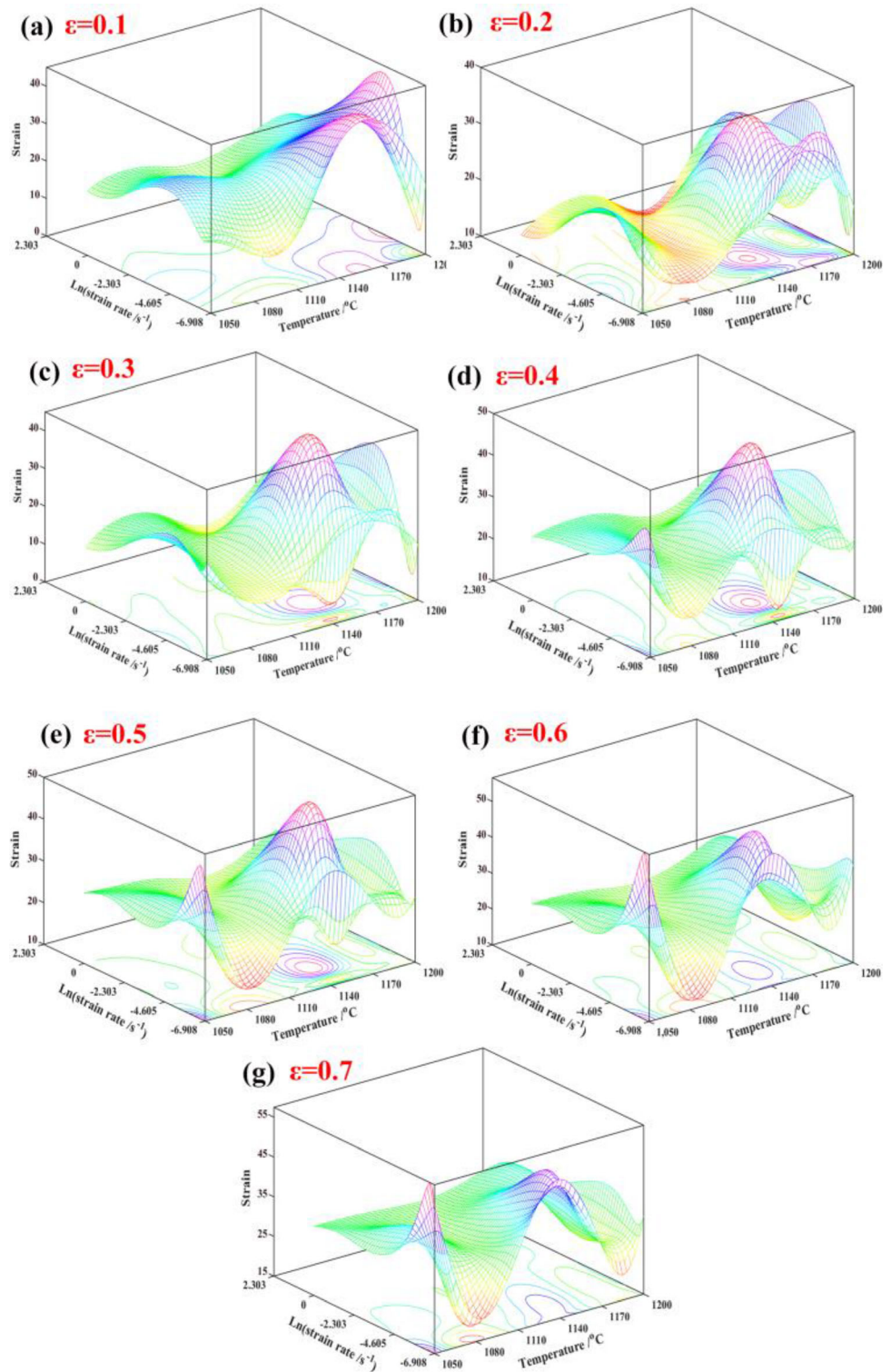


**Figure 15** The evolution of 2D contour maps of power dissipation efficiency with increasing strain at different deformation conditions.

**Figure 16** The evolution of 3D distribution of power dissipation efficiency with increasing strain at different processing parameters.



in higher temperature intervals. For a certain deformation temperature of 1050 °C, the  $\eta$  values increase with the increasing strain irrespective of strain rate. Thus, the higher  $\eta$  values is mainly located in higher

strain intervals of 0.4–0.7. Compared with high strain rate, the higher  $\eta$  values can be obtained at low strain rate.



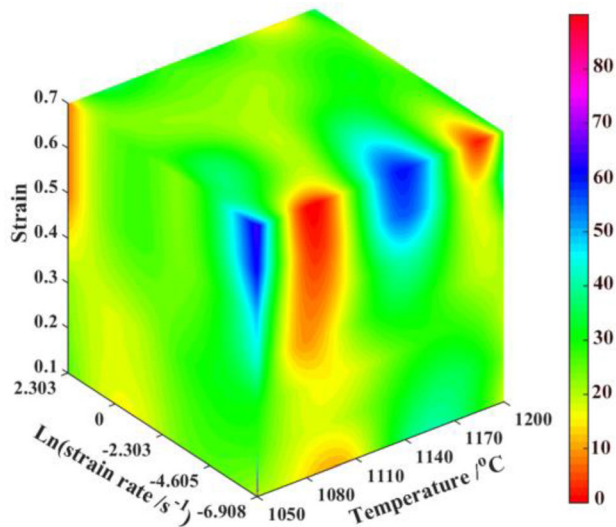


**Figure 17** The 3D power dissipation efficiency map in the processing region.

#### Evolution of 3D instability maps with strain

The 3D flow instability maps composed by 2D plane instability maps at the strain range of 0.1–0.7 with an interval of 0.1 are displayed in Fig. 18, where the instability region and stability region are represented by blue and red, respectively. It is clear that the flow instability map is sensitive to the strain level and the proportion of instability region is much smaller than that of stability region. It can be seen from Fig. 18 that the flow instability tends to exist in the lower deformation temperature and higher strain rate region. The instability region corresponds to the 1050–1090 °C and 0.45–10 s<sup>-1</sup> temperature and strain rate intervals at initial strain of 0.1. With the further increase of strain, the instability region gradually expands to higher temperature and lower strain rate. The instability region is also found in the temperature

range of 1155–1200 °C and strain rate range of 1–10 s<sup>-1</sup> until the strain reaches 0.5. The two instability regions mentioned above gradually expand with the increase of strain. When the strain reaches 0.7, the two instability regions merge into one instability region, that is, at a strain of 0.7 and the strain rate intervals of 1–10 s<sup>-1</sup>, the instability region exists almost in the entire deformation temperature of 1050–1195 °C. Additionally, at a lower strain rate, there are two smaller instability regions in the temperature range of 1070–1090 °C and 1140–1170 °C.

#### Evolution of 3D processing maps with strain

The processing maps of EP741NP superalloy are established by superimposing the instability maps on power dissipation efficiency maps at different strains, as shown in Fig. 19. The numbers on the contour line in processing maps represent the values of power dissipation efficiency ( $\eta$ ), and the shaded areas indicate the instability regions with negative  $\xi$  values as depicted based on the criterion given in Eq. (24), while the white areas are stability regions. The determination of the optimal processing parameters requires comprehensive consideration of power dissipation efficiency and flow instability. It can be seen from Fig. 19a that at the initial strain of 0.1, the power dissipation efficiency with a value of more than 35% exhibits in two regions, which occurs in the areas of 1135–1180 °C/0.001–0.003 s<sup>-1</sup> and 1190–1200 °C/0.004–0.030 s<sup>-1</sup>. Further increasing the strain, these two higher  $\eta$  value regions gradually expand to low temperature and high strain rate. When the samples deformed at strain of 0.4, the higher  $\eta$  value region over 35% is also concentrated in the temperature range of 1050–1055 °C and strain rate range of 0.001–0.0025 s<sup>-1</sup>. As the strain increases, this region

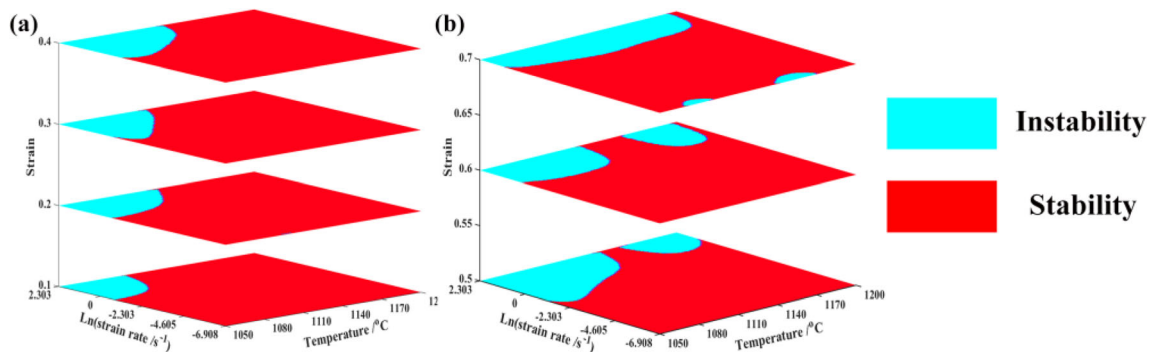
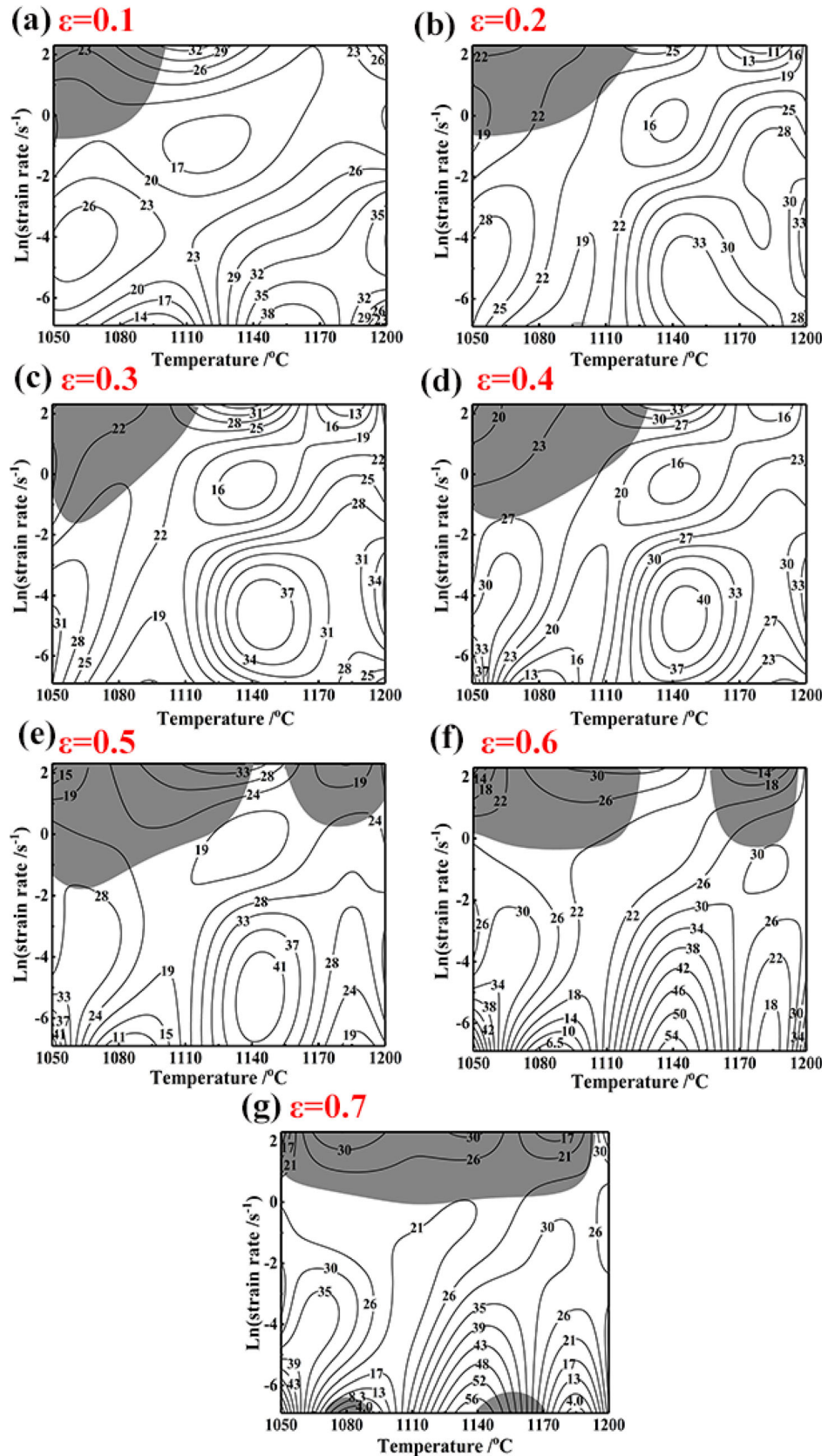


**Figure 18** The 3D flow instability maps of EP741NP superalloy composed by 2D plane instability maps at different strains.



**Figure 19** Processing maps of EP741NP superalloy at different strains.



extends to the higher deformation temperature and higher strain rate, and the  $\eta$  value also increases significantly. Moreover, it must be pointed out that the three main deformation mechanisms which exist in the stability region, including DRV, DRX and superplasticity are closely related to the magnitude of the power dissipation efficiency value. Generally, DRX is considered as the best option for hot deformation [43], the  $\eta$  value with respect to DRX is about 30–50%, while the  $\eta$  value related to DRV is about 15–25%, the value associated with superplasticity is greater than 60% [9, 44]. Based on the variation of  $\eta$  value in Fig. 19, it may be further inferred that the superplasticity would not occur in working process, and DRX and DRV metallurgical processes may exist in whole hot deformation process.

At present, most of the research on the hot workability of materials tends to employ the processing map obtained at higher strain. Herein, the dominant deformation mechanism of a specific area in the processing map at strain of 0.7 is investigated by combining the deformed microstructure during hot deformation. The whole processing map can be broadly divided into four domains which are marked as A–D in Fig. 20 based on the instability regions and the value of power dissipation efficiency; thereinto, Domains A and B are located in the instability region, Domain C is the stability region with the  $\eta$  value of less than 26%, while the stability region with the  $\eta$  value of more than 26% is identified to be Domain D.

- (1) Domain A, with the  $\eta$  of 17–30% and negative  $\zeta$ , occurs in the temperature range of 1050–1195 °C and strain rate of 1–10 s<sup>-1</sup>. The representative microstructure at temperature of 1080 °C with strain rate of 10 s<sup>-1</sup> shows obvious wedge microcracks and shear bands during hot deformation. It is noteworthy that the shear band and the compression direction are approximately at an angle of 45°, which is basically consistent with the results mentioned in the study of the hot deformation behavior of Inconel 718 alloy by F. Sui et al. [45]. This is because the low temperature leads to a decrease in atomic activity, and most slip systems are not activated; meanwhile, there is not enough time for plastic deformation and softening owing to high strain rate [9]. Consequently, it is not suitable to perform hot working on EP741NP superalloy at low temperature and high strain rate. The hot-pressed samples deformed at temperature of 1170 °C with strain rate of 10 s<sup>-1</sup>, and the cracks mainly occur at the grain boundaries. This may be due to the fact that the unit length of grain boundary decreases with the increase of temperature at a higher strain rate and deformation temperature, and the stress concentration generated at grain boundary is not released in time [46]. In addition, the inhomogeneous microstructure deformed at 1080 °C/10 s<sup>-1</sup> consisting of a large number of elongated and distorted grains perpendicular to the compression direction can be observed in this region. At a higher strain rate, the heat generated by plastic deformation does not have enough time to transfer to the cold area, resulting in uneven temperature distribution of the compressed specimen [9].
- (2) Domain B, a narrow flow instability region, locates in the temperature range of 1070–1170 °C and strain rate of 0.001–0.0025 s<sup>-1</sup>. It should be noted that traditional instability characteristics, such as intercrystalline cracks, shear band and flow localized slip, are not observed in the microstructure of this domain. On the contrary, it is similar to the microstructure of stability region, showing complete DRX. This phenomenon is consistent with the results reported by Pu et al. [7]. It may be due to dynamic strain aging and secondary work hardening occurring in this region to cause flow instability.
- (3) Domain C contains two parts (Domain C1 and Domain C2). Domain C1 is located in the temperature range of 1050–1160 °C and strain rate range of 0.001–2.718 s<sup>-1</sup> with the  $\eta$  value range of 4.3–22%. Domain C2 is located in the range of 1170–1200 °C/0.001–0.03 s<sup>-1</sup> with the  $\eta$  value range of 4.3–26%. In Domain C1, the typical microstructure deformed at 1110 °C/0.01 s<sup>-1</sup>, 1110 °C/1 s<sup>-1</sup> and 1140 °C/1 s<sup>-1</sup> is displayed in this region. It is not difficult to find that the fraction of DRX increases with the increase of the deformation temperature and the decrease of the strain rate by comparing the microstructure under the above three deformation conditions. Moreover, only a small part of the DRX grains on the grain boundary can be observed in the microstructure of this domain. However, Domain C1 should be avoided in hot

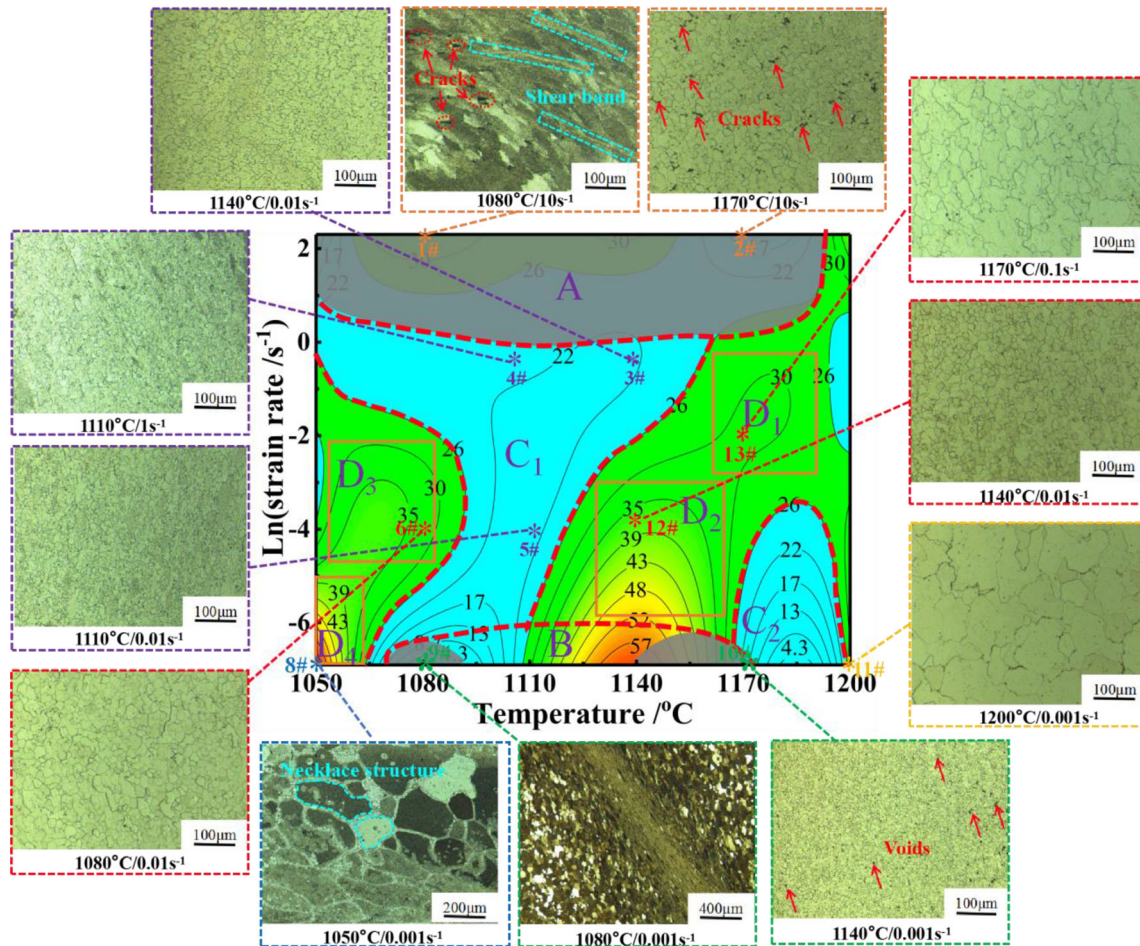


**Figure 20** Processing map of EP741NP superalloy at strain of 0.7 with microstructure validation in different deformation domains.

deformation because the microstructure characteristics of incomplete DRX are detrimental to obtaining uniform microstructure and good mechanical properties. For Domain C2 located at high temperature and low strain rate, complete DRX can be found under such deformation parameters and DRX grains grows significantly, which is in good agreement with the microstructure deformed at 1200 °C/0.001 s<sup>-1</sup>. The volume fraction of γ' precipitate also decreases obviously, indicating γ' precipitate was partially dissolved during hot working. Besides, the η values in the Domain C1 and C2 changes drastically, which means that the energy transmission in hot deformation is heterogeneous. Thus, Domain C should not be recommended to be desirable hot working window.

- (4) Domain D spreads over the temperature range of 1050–1200 °C and strain rate range of 0.001–

1 s<sup>-1</sup> except Domains B and C. This domain is composed of four stability regions (D1, D2, D3 and D4) with high power dissipation efficiency range of 26–52%. DRX is expected to be the dominant microstructure mechanism in this region. The representative microstructures deformed at 1170 °C/0.1 s<sup>-1</sup>, 1140 °C/0.01 s<sup>-1</sup> and 1080 °C/0.01 s<sup>-1</sup> all show homogeneous and fully recrystallized characteristics without deformation defects corresponding to Domain D1, Domain D2 and Domain D3, respectively. In brief, the original microstructure is replaced by fine equiaxed dynamic recrystallized grains. Domain D4 lies in the temperature range of 1050–1065 °C and strain rate range of 0.001–0.0067 s<sup>-1</sup> with the peak power dissipation efficiency of 43%, the microstructure mechanism in this domain should be theoretically dominated by DRX, but the typical necklace structure is found, as shown in microstructure



deformed at 1050 °C/0.001 s<sup>-1</sup>. It can be seen that from Fig. 21 that necklace structure is composed of larger deformed grains and some fine DRX grains; the shape is similar to necklace. It is worth noting that the boundaries of deformed grains show bulging, which indicates that DRX appears; that is, the nucleation of DRX is carried out by bulging of deformed grain boundaries [47]. E. Pu et al. [7] pointed out that in the early stage of deformation, rapid strain hardening occurred due to the increase of dislocation density, which formed the grain boundary bulging. During the hot compression process, DRX nucleation occurs better at the triple junctions and the initial grain boundaries, thus forming a necklace structure. It is not recommended as the optimal hot processing window in Domain D4. Accordingly, optimum processing condition for EP741NP superalloy in this study is considered to be Domain D1 (1160–1190 °C/0.05–0.819 s<sup>-1</sup>), D2 (1130–1165 °C/0.0025–0.05 s<sup>-1</sup>) and D3 (1055–1085 °C/0.011–0.135 s<sup>-1</sup>).

## Conclusions

In this work, the hot deformation behaviors and workability of nickel-based EP741NP superalloy were investigated by hot compression tests performed at temperatures of 1050–1200 °C and strain rates of 0.001–10 s<sup>-1</sup>. Basically, the following conclusions can be drawn:

- (1) The experimental flow stress data were corrected by friction and adiabatic heating effect under all deformation parameters. Dynamic

recrystallization as the dominant softening behavior tends to strengthen as strain rate increases and deformation temperature decreases.

- (2) Based on Arrhenius-type model, the coupling effect of deformation temperature and strain rate on corrected flow stress can be described by the Zener–Hollomon parameter, and the hot deformation activation energy was determined as 577.45 kJ/mol. Consequently, the constitutive equations of EP741NP alloy can be established in combination with DRX critical model and kinetics model as follows:

$$\begin{cases} \sigma = [\sigma_{sat}^2 + (\sigma_{0.2}^2 - \sigma_{sat}^2)\exp(-r(\epsilon - \epsilon_{0.2}))]^{1/2}, \epsilon < \epsilon_c \\ \sigma = [\sigma_{sat}^2 + (\sigma_{0.2}^2 - \sigma_{sat}^2)\exp(-r(\epsilon - \epsilon_{0.2}))]^{1/2} - X_{DRX}(\sigma_{sat} - \sigma_{ss}), \epsilon \geq \epsilon_c \end{cases}$$

$$\begin{cases} X_{DRX} = 0, \epsilon < \epsilon_c \\ X_{DRX} = 1 - \exp\{-0.2344[(\epsilon - \epsilon_c)/\epsilon_p]^{1.2566}\}, \epsilon \geq \epsilon_c \end{cases}$$

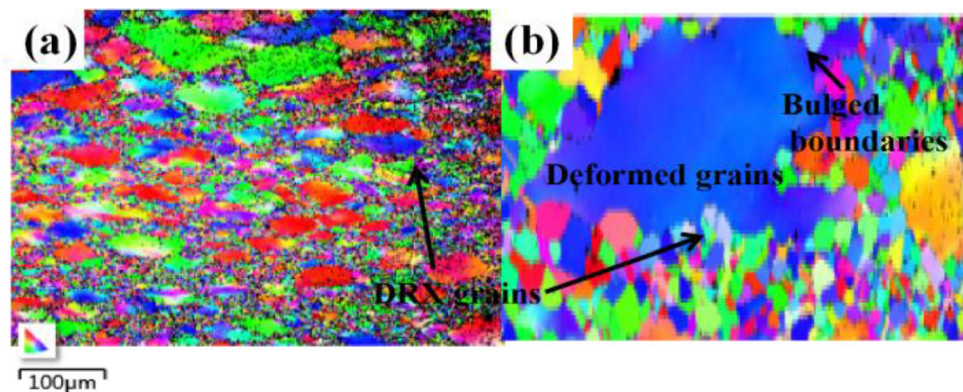
$$\begin{cases} \sigma_p = 2.339\sigma_c^{0.87} \\ \sigma_p = 0.00003Z^{0.32} \end{cases} \begin{cases} \epsilon_p = 1.44\epsilon_c^{0.99} \\ \epsilon_p = 0.0034Z^{0.06} \end{cases}$$

$$\begin{cases} \sigma_c = 0.376\sigma_p - 22.859 \\ \sigma_{0.2} = 0.954\sigma_p - 10.217 \\ \sigma_{sat} = 1.012\sigma_p - 0.667 \\ \sigma_{ss} = 0.527\sigma_p - 7.184 \\ \lg r = -9.512 \times 10^4 + 2.02 \end{cases}$$

$$\begin{aligned} Z &= \dot{\epsilon} \exp(577450/RT) \\ &= 5.081 \times 10^{22} [\sinh(0.003995\sigma_p)]^{3.581} \end{aligned}$$

- (3) There is good consistency between the flow stress calculated by the constitutive equation and experimental data, with the correlation coefficient (R) of 99% and the average absolute relatively error (AARE) of 8.73%. In addition, the DRX kinetic model was validated by EBSD microstructure observation.

**Figure 21** IPF maps of samples hot compressed at 1050 °C/0.001 s<sup>-1</sup> **a** and magnification diagram of necklace structure **b**.





(4) Based on the 3D processing maps and microstructure verification, the optimum hot deformation windows, in which EP741NP superalloy displayed a significant DRX with uniform and fine grains, were determined to be Domain  $D_1(1160\text{--}1190\text{ }^\circ\text{C}/0.05\text{--}0.819\text{ s}^{-1})$ , Domain  $D_2(1130\text{--}1165\text{ }^\circ\text{C}/0.0025\text{--}0.05\text{ s}^{-1})$  and Domain  $D_3(1055\text{--}1085\text{ }^\circ\text{C}/0.011\text{--}0.135\text{ s}^{-1})$ .

## Acknowledgements

This work was sponsored by the National Natural Science Foundation of China (Grant No. 51405110), the China Postdoctoral Science Foundation (Grant No. 2014M551234), the Specialized Research Fund for the Doctoral Program of Higher Education (Grant No. 20132302120002) and the Fundamental Research Funds for the Central Universities (Grant No. HIT.NSRIF.2014006).

## Declarations

**Conflict of interest** The authors declare that they have no known competing financial interests or personal relationships that could have appeared to influence the work reported in this paper.

## References

- [1] Ganeev AA, Valitov VA, Utyashev FZ, Imaev VM (2019) The influence of temperature-strain rate conditions on hot workability and microstructure of powder metallurgy nickel-based superalloy EP741NP. *Phys Met Metallogr* 120:410–416
- [2] Kumar SSS, Raghu T, Bhattacharjee PP, Rao GA, Borah U (2017) Work hardening characteristics and microstructural evolution during hot deformation of a nickel superalloy at moderate strain rates. *J Alloys Compd* 709:394–409
- [3] Rastegari H, Kermanpur A, Najafizadeh A, Somani CM, Porter AD, Ghassemali E (2016) Determination of processing maps for the warm working of vanadium microalloyed eutectoid steels. *Mater Sci Eng A* 658:167–175
- [4] Wu H, Wen S, Huang H, Wu X, Gao K, Wang W, Nie ZR (2016) Hot deformation behavior and constitutive equation of a new type Al-Zn-Mg-Er-Zr alloy during isothermal compression. *Mater Sci Eng A* 651:415–424
- [5] Qin X, Huang D, Yan X, Zhang X, Qi M, Yue S (2018) Hot deformation behaviors and optimization of processing parameters for Alloy 602 CA. *J Alloys Compd* 770:507–516
- [6] Lin Y, Nong F, Chen X, Chen D, Chen M (2017) Microstructural evolution and constitutive models to predict hot deformation behaviors of a nickel-based superalloy. *Vacuum* 137:104–114
- [7] Pu E, Zheng W, Song Z, Feng H, Dong H (2017) Hot deformation characterization of nickel-based superalloy UNS10276 through processing map and microstructural studies. *J Alloys Compd* 15:617–631
- [8] Wu H, Liu M, Wang Y, Huang Z, Tan G, Yang L (2020) Experimental study and numerical simulation of dynamic recrystallization for a FGH96 superalloy during isothermal compression. *J Mater Res Technol* 9:5090–5104
- [9] Wang M, Wang W, Liu Z, Sun C, Qian L (2018) Hot workability integrating processing and activation energy maps of Inconel 740 superalloy. *Mater Today Commun* 14:188–198
- [10] Wen D, Lin Y, Chen J, Deng J, Chen X, Zhang J, He M (2015) Effects of initial aging time on processing map and microstructures of a nickel-based superalloy. *Mater Sci Eng A* 620:319–332
- [11] Oleksandr L, Tomasz S, Krystian Z, Aneta L, Marek W (2020) Evaluation of Hot Workability of Nickel-Based Superalloy Using Activation Energy Map and Processing Maps. *Materials* 13(16):3629
- [12] Wu Z, Tang Y, Chen W, Lu L, Li E, Li Z, Ding H (2019) Exploring the influence of Al content on the hot deformation behavior of Fe-Mn-Al-C steels through 3D processing map. *Vacuum* 159:447–455
- [13] Liu Y, Ning Y, Yang X, Yao Z, Guo H (2016) Effect of temperature and strain rate on the workability of FGH4096 superalloy in hot deformation. *Mater Design* 95:669–676
- [14] Ke B, Ye L, Tang J, Zhang Y, Liu S, Lin H, Dong Y, Liu X (2020) Hot deformation behavior and 3D processing maps of AA7020 aluminum alloy. *J Alloys Compd* 845:156113
- [15] Ji H, Duan H, Li Y, Li Y, Li W, Huang X, Pei W, Lu Y (2020) Optimization the working parameters of as-forged 42CrMo steel by constitutive equation-dynamic recrystallization equation and processing maps. *J Mater Res Technol* 9:7210–7224
- [16] Wu R, Liu Y, Geng C, Lin Q, Xiao Y, Xu J, Kang W (2017) Study on hot deformation behavior and intrinsic workability of 6063 aluminum alloys using 3D processing map. *J Alloys Compd* 713:212–221
- [17] Ebrahimi R, Najafizadeh A (2004) A new method for evaluation of friction in bulk metal forming. *J Mater Process Tech* 152:136–143

- [18] Goetz RL, Semiatin SL (2001) The adiabatic correction factor for deformation heating during the uniaxial compression test. *J Mater Eng Perform* 10:710–717
- [19] Oh SI, Semiatin SL, Jonas JJ (1992) An analysis of the isothermal hot compression test. *Metall Trans A* 23:963–975
- [20] Academic Committee of the Superalloys (2012) CMS, China superalloys handbook: part I. China Zhijian Publishing House, Standards Press of China
- [21] Wan Z, Hu L, Sun Y, Wang T, Li Z (2018) Hot deformation behavior and processing workability of a Ni-based alloy. *J Alloys Compd* 769:367–375
- [22] Maj P, Zdunek J, Mizera J, Kurzydowski K, Sakowicz B, Kaminski M (2017) Microstructure and strain-stress analysis of the dynamic strain aging in inconel 625 at high temperature. *Met Mater Int* 23:54–67
- [23] Mahalle G, Kotkunde N, Gupta A, Singh S (2019) Analysis of hot workability of inconel alloys using processing maps[M]
- [24] Liu Y, Ning Y, Yao Z, Li H, Miao X, Li Y, Zhao Z (2016) Plastic deformation and dynamic recrystallization of a powder metallurgical nickel-based superalloy. *J Alloys Compd* 675:73–80
- [25] Shen J, Hu L, Sun Y, Fang A, Wan Z (2020) Hot deformation behaviors and three-dimensional processing map of a nickel-based superalloy with initial dendrite microstructure. *J Alloys Compd* 822:153735
- [26] Tan Y, Ma Y, Zhao F (2018) Hot deformation behavior and constitutive modeling of fine grained Inconel 718 superalloy. *J Alloys Compd* 741:85–96
- [27] Zhang Y, Han S, Jia J, Liu J, Hu B (2015) Effect of microelement Hf on the microstructure of powder metallurgy superalloy FGH97. *Acta Metall Sin* 51(10):1219–1226
- [28] Xu Z, Li H, Li M (2017) Dynamic recrystallization model of GH696 superalloy. *Zhongguo Youse Jinshu Xuebao Chin J Nonferr Metals* 27:1551–1562
- [29] Mcqueen HJ, Ryan ND (2002) Constitutive analysis in hot working. *Mater Sci Eng A* 322:43–63
- [30] Ryan ND, Mcqueen HJ (1990) Dynamic Softening Mechanisms in 304 Austenitic Stainless Steel. *Can Metall Quart* 29:147–162
- [31] Poliak EI, Jonas JJ (1996) A one-parameter approach to determining the critical conditions for the initiation of dynamic recrystallization. *Acta Mater* 44:127–136
- [32] Mirzadeh H, Cabrera JM, Najafizadeh A (2012) Modeling and Prediction of Hot Deformation Flow Curves. *Metall Mater Trans A* 43:108–123
- [33] Jonas JJ, Quelennec X, Jiang L, Martin É (2009) The Avrami kinetics of dynamic recrystallization. *Acta Mater* 57:2748–2756
- [34] Laasraoui A, Jonas JJ (1991) Recrystallization of austenite after deformation at high temperatures and strain rates analysis and modeling. *Metall Mater Trans A* 22:151–160
- [35] Serajzadeh S, Taheri AK (2003) Prediction of flow stress at hot working condition. *Mech Res Commun* 30:87–93
- [36] Kotkunde N, Deole AD, Gupta AK, Singh SK (2014) Comparative study of constitutive modeling for Ti-6Al-4V alloy at low strain rates and elevated temperatures. *Mater Des* 55:999–1005
- [37] Prasad YVRK, Gegel HL, Doraivelu SM, Malas JC, Morgan JT (1984) Modeling of dynamic material behavior in hot deformation: Forging of Ti-6242. *Metall Trans A* 15:1883–1892
- [38] Prasad YVRK, Seshacharyulu T (1998) Modelling of hot deformation for microstructural control. *Metall Rev* 43:243–258
- [39] Prasad YVRK (1990) Recent advances in the Science of Mechanical processing. *Indian J Technol* 28:435–451
- [40] Murty SVSN, Rao BN (1998) Ziegler's criterion on the instability regions in processing maps. *J Mater Sci Lett* 17:1203–1205
- [41] Gopinath K, Gogia AK, Kamat SV, Ramamurty U (2009) Dynamic strain ageing in Ni-base superalloy 720Li. *Acta Mater* 57:1243–1253
- [42] Seshacharyulu T, Medeiros SC, Frazier WG, Prasad YVRK (2000) Hot working of commercial Ti-6Al-4V with an equiaxed a-b microstructure: materials modeling considerations. *Mater Sci Eng A* 284:184–194
- [43] Ning Y, Yao Z, Li H, Guo H, Tao Y, Zhang Y (2010) High temperature deformation behavior of hot isostatically pressed P/M FGH4096 superalloy. *Mater Sci Eng A* 527:961–966
- [44] Chiba A, Lee SH, Matsumoto H, Nakamura M (2009) Construction of processing map for biomedical Co-28Cr-6Mo-0.16N alloy by studying its hot deformation behavior using compression tests. *Mater Sci Eng A* 514:286–293
- [45] Sui F, Xu L, Chen L, Liu X (2011) Processing map for hot working of Inconel 718 alloy. *J Mater Process Tech* 211:433–440
- [46] Zeng SW, Zhao AM, Jiang HT, Ren Y (2017) Flow behavior and processing maps of Ti-44.5Al-3.8Nb-1.0Mo-0.3Si-0.1B alloy. *J Alloys Compd* 698:786–793
- [47] Yu Q, Yao Z, Dong J (2015) Deformation and Recrystallization Behavior of a Coarse-Grain, Nickel-Base Superalloy Udimet720Li Ingot Material. *Mater Charact* 107:398–410

**Publisher's Note** Springer Nature remains neutral with regard to jurisdictional claims in published maps and institutional affiliations.